

1-1-2007

Design of sputtering system for hemispherical boron 10 target

Priya Raman

University of Nevada, Las Vegas

Follow this and additional works at: <https://digitalscholarship.unlv.edu/rtds>

Repository Citation

Raman, Priya, "Design of sputtering system for hemispherical boron 10 target" (2007). *UNLV Retrospective Theses & Dissertations*. 2185.
<http://dx.doi.org/10.25669/pumy-gv0l>

This Thesis is protected by copyright and/or related rights. It has been brought to you by Digital Scholarship@UNLV with permission from the rights-holder(s). You are free to use this Thesis in any way that is permitted by the copyright and related rights legislation that applies to your use. For other uses you need to obtain permission from the rights-holder(s) directly, unless additional rights are indicated by a Creative Commons license in the record and/or on the work itself.

This Thesis has been accepted for inclusion in UNLV Retrospective Theses & Dissertations by an authorized administrator of Digital Scholarship@UNLV. For more information, please contact digitalscholarship@unlv.edu.

DESIGN OF SPUTTERING SYSTEM FOR HEMISPHERICAL BORON 10 TARGET

by

Priya Raman

Bachelor of Engineering
Bharathidasan University
Tamil Nadu, India
2004

A thesis submitted in partial fulfillment
of the requirements for the

Master of Science Degree in Electrical Engineering
Department of Electrical and Computer Engineering
Howard R. Hughes College of Engineering

Graduate College
University of Nevada Las Vegas
August 2007

UMI Number: 1448417

INFORMATION TO USERS

The quality of this reproduction is dependent upon the quality of the copy submitted. Broken or indistinct print, colored or poor quality illustrations and photographs, print bleed-through, substandard margins, and improper alignment can adversely affect reproduction.

In the unlikely event that the author did not send a complete manuscript and there are missing pages, these will be noted. Also, if unauthorized copyright material had to be removed, a note will indicate the deletion.

UMI[®]

UMI Microform 1448417

Copyright 2007 by ProQuest Information and Learning Company.

All rights reserved. This microform edition is protected against unauthorized copying under Title 17, United States Code.

ProQuest Information and Learning Company
300 North Zeeb Road
P.O. Box 1346
Ann Arbor, MI 48106-1346



Thesis Approval
The Graduate College
University of Nevada, Las Vegas

July 20, 20 07

The Thesis prepared by

Priya Raman

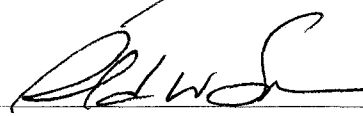
Entitled

Design of Sputtering System for Hemispherical Boron 10 Target

is approved in partial fulfillment of the requirements for the degree of


Master of Science in Electrical Engineering


Examination Committee Chair


Dean of the Graduate College


Examination Committee Member


Examination Committee Member


Graduate College Faculty Representative

ABSTRACT

Design of Sputtering System for Hemispherical Boron 10 Target

by

Priya Raman

Dr. Rama Venkat, Examination Committee Chair
Professor, Electrical and Computer Engineering
University of Nevada, Las Vegas

^{10}B is an isotope of Boron. ^{10}B and neutron interaction yields alpha particles. α particles typically deposit their energy within a few tenths of nanometers within a semiconductor creating electron-hole pairs which through radiative recombination yield photon emission of band gap energy. The number of photons emitted directly relates to the energy and flux density of incoming neutron. Thus, ^{10}B coated semiconductors can be used as a neutron detectors. ^{10}B is an expensive material, especially in the disc and the powdered form which is needed for sputtering. Since a hemispherical target of ^{10}B of diameter 4.8cm was available, a sputter source was designed and built around this target. The design was based on various electrostatic and magnetostatic analysis from TRICOMP 6.0(Finite Element Software for Electromagnetics), SOLIDWORKS 2006(3 D Mechanical Design Software) and previous experience with sputtering systems and vacuum systems. The vacuum chamber was evacuated by an unthrottled turbomolecular pump backed by an oil sealed mechanical

pump. The target head consists of ^{10}B , cylindrical soft iron housing with a glass ring to prevent sputtering of iron from the stainless steel ring and Neodymium-Iron-Boron permanent magnet. Thin films of ^{10}B were deposited on silicon wafer and were characterized for its chemical composition and thickness using X-ray fluorescence spectroscopy and Scanning electron Microscope. The growth rate was in the range of $0.046\text{\AA}/\text{sec}$. The deposited film contained ^{10}B in the range of 19.46 %, carbon in the range of 1.31% and copper in the range of 14.21%. In addition to all these elements, the films contained 65 % of oxygen. Despite the fact that the system was leak tight (as determined by a quadrupole mass analyzer), the presence of oxygen in the deposited films could not be avoided. This was due to residual water vapor and our necessarily low deposition rate. This was further ascertained by a theoretical calculation based on RGA measurements and growth rate. Possible improvements to system are: rotating the substrate to improve spatial thickness uniformity, cooling the sputter head so that the deposition rate can be increased and changing the rubber o-ring so that the system can be baked to minimize oxygen incorporation in the film.

TABLE OF CONTENTS

ABSTRACT	iii
LIST OF FIGURES	vii
ACKNOWLEDGEMENTS.....	x
CHAPTER 1 INTRODUCTION.....	1
1.1 Organization of the Thesis.....	3
CHAPTER 2 NEUTRON DETECTORS.....	4
2.1 Principle of Operation	4
2.2 Device Structure	6
2.2.1 Boron Deposition	7
2.2.1.2 Sputtering.....	8
2.2.1.3 Chemical Vapor Deposition	9
2.2.2 Theoretical Considerations and Detector Design.....	10
2.2.2.1 ¹⁰ B Film Coatings and Efficiency.....	10
2.2.2.2 Diode Structures	10
2.3 Monte Carlo N-Particle Simulation(Theoretical analysis).....	11
2.4 Device/Detector Results [15]	13
CHAPTER 3 PLASMA AND SPUTTERING.....	14
3.1 Plasma.....	14
3.1.1 Introduction to Glow Discharges	17
3.1.1.1 Direct current (DC) glow discharge	18
3.1.1.2 Radio Frequency (RF) glow discharge	24
3.2 Sputtering.....	27
3.2.1 Physics of Sputtering.....	28
3.2.2 Magnetron Sputtering.....	29
CHAPTER 4 VACUUM SYSTEMS AND INSTRUMENTS USED IN THIN FILM CHARACTERIZATION AND LEAK DETECTION	32
4.1 Vacuum Systems	32
4.1.1 Vacuum Pumping Mechanisms.....	33
4.1.1.1 Mechanical Pumps/Roughing Pumps.....	34
4.1.1.2 Turbomolecular Pumps.....	35
4.1.2 Vacuum Chamber.....	36
4.1.3 Pressure Gauges	37
4.1.3.1 Convectron Gauge	37

4.1.3.2 Ionization Gauge.....	38
4.1.4 Target.....	39
4.1.5 Sputter Head	40
4.1.6 Power Supply	42
4.2 Instruments used for Thin Film characterization and leak detection	42
4.2.1 X Ray Photoelectron spectroscopy (XPS).....	43
4.2.2 Scanning Electron Microscopy (SEM).....	45
4.2.3 Quadrupole Gas Analyzer/Residual Gas Analyzer	48
CHAPTER 5 DESIGN OF SPUTTERING SYSTEM.....	51
5.1 Paper Design.....	51
5.1.1 SOLIDWORKS 2006.....	52
5.1.2 TRICOMP 6.0	57
5.2 Manufacture of Components	61
5.3 Experimental Procedure	67
CHAPTER 6 RESULTS AND DISCUSSIONS	69
6.1 Results	69
6.2 Discussions	77
CHAPTER 7 CONCLUSION AND RECOMMENDATIONS	82
7.1 Conclusions	82
7.2 Recommendations for Future Work	83
APPENDIX.....	84
BIBLIOGRAPHY.....	86
VITA.....	90

LIST OF FIGURES

Figure 2. 1	A Schematic diagram of the reaction governing the boron based neutron detectors.....	5
Figure 2. 2	A Schematic diagram showing the location of various nuclear interactions in a solid state neutron detector.	7
Figure 2. 3	A Schematic diagram of the device structure.	11
Figure 2. 4	A plot of Efficiency Vs Film thickness from MCNP.	12
Figure 3. 1	A schematic representation of the four states of matter.	15
Figure 3. 2	A figure showing schematic diagram of plasma.	15
Figure 3. 3	A photograph showing thermal plasma.	16
Figure 3. 4	A figure showing glow discharge plasma.....	17
Figure 3. 5	A figure showing schematic drawing of a dc glow discharge established in a glass tubes containing a gas under reduced pressure.....	19
Figure 3. 6	A figure showing the paschen curve.....	20
Figure 3. 7	A schematic figure showing (a) charge density of ions and electrons (b) plasma and dark regions and (c) electrostatic potential as a function of location between the anode and the cathode.	22
Figure 3. 8	A Schematic figure showing electrostatic potential versus distance between the two electrodes.....	25
Figure 3. 9	A schematic diagram illustrating the steps in sputtering process.	27
Figure 3. 10	A picture showing the sputter environment.....	29
Figure 3. 11	A schematic picture illustrating the Magnetron sputtering process	30
Figure 3. 12	A photograph showing the electron confinement which causes a non-uniform erosion of the target in magnetron sputtering	31
Figure 4. 1	Photographs of (a) Oil sealed rotary vane pump, (b) a cross sectional view	35
Figure 4. 2	A photograph showing the cross sectional view of a Turbomolecular pump.	36
Figure 4. 3	A picture showing a typical vacuum chamber.....	37
Figure 4. 4	A photograph of a Digital Convectron Gauge Controller	38
Figure 4. 5	A photograph showing an Ionization Gauge.	39
Figure 4. 6	A photograph showing conventional targets.	40
Figure 4. 7	A picture showing three conventional sputter heads.....	41
Figure 4. 8	A photograph of a DC Magnetron Power Supply.	42
Figure 4. 9	An XPS spectrum obtained from a Pd metal sample using Mg K α radiation.	44
Figure 4. 10	A photograph showing our XPS setup.	45
Figure 4. 11	A photograph showing a typical SEM.....	48

Figure 4. 12	A photograph showing a typical RGA.	50
Figure 5. 1	Mechanical drawings of the SS-410 stainless steel cylinder.	53
Figure 5. 2	Mechanical drawings of the copper ring.	53
Figure 5. 3	Mechanical drawings of the hemispherical Boron 10 dome.	54
Figure 5. 4	A mechanical drawings of the aluminum sleeve used for sliding the permanent magnet in to its place in the SS-410 cylinder.	55
Figure 5. 5	A 3-D view of the Aluminum sleeve with SS-410.	56
Figure 5. 6	A 3-D view showing the arrangement of the sputter head set-up.	56
Figure 5. 7	A 3-D view of the sputter head set-up with the hemispherical target.	57
Figure 5. 8	A 2-D view of the mesh generated for the sputtering setup using MESH 6.0 program of TRICOMP 6.0.	58
Figure 5. 9	A 2-D view of the electrostatic field lines generated using ESTAT 6.0 for the sputtering setup.	59
Figure 5. 10	A 2-D view of the magnetic field lines generated using PERMAG 6.0 for the sputtering setup.	60
Figure 5. 11	A photograph showing how the Aluminum sleeve fits in SS-410 cylinder.	62
Figure 5. 12	A photograph depicting the placing of the permanent magnet on SS-410.	63
Figure 5. 13	A photograph of the permanent magnet placed exactly in the middle of the	63
Figure 5. 14	A photograph of the copper ring with the ^{10}B dome on the top of it.	64
Figure 5. 15	A photograph showing the sputter head set-up with copper rod, SS-410, copper ring and the hemispherical boron 10 dome.	65
Figure 5. 16	A picture showing target set up with the copper rod.	65
Figure 5. 17	A photograph of the side view of the sputter chamber showing the vertically suspended sputter head.	66
Figure 5. 18	A photographic view of the top portion of the sputter chamber with the turbo pump and high vacuum gauge.	66
Figure 5. 19	A photographic view of the complete sputtering system showing the mechanical pump.	67
Figure 5. 20	A schematic block diagram of the whole sputtering system.	68
Figure 5. 21	A photographic view of the complete sputtering system with the power supply.	68
Figure 6. 1	A photograph of an SEM image showing the thickness of the deposited ^{10}B film at a magnification of 25,000X.	70
Figure 6. 2	A photograph of an SEM image showing the thickness of the deposited ^{10}B film at a magnification of 11,000X.	70
Figure 6. 3	EDS high-resolution plot of energy (eV) versus counts per second obtained from sputtered film.	71
Figure 6. 4	EDS high-resolution plot of energy (eV) versus counts per second obtained from sputtered film.	72
Figure 6. 5	XPS spectra of binding energy versus counts for a typical sample without the glass ring.	73
Figure 6. 6	A photograph showing sputter head set-up with the glass ring.	76

Figure 6. 7	XPS spectra of binding energy versus counts for a typical sample with the glass ring.....	74
Figure 6. 8	XPS spectra of binding energy versus counts for hemispherical ¹⁰ B target.	75
Figure 6. 9	Quadrupole gas analyzer spectrum of $\frac{\text{Mass}}{\text{Charge}}$ ratio versus partial pressure with Ar flow.....	76
Figure 6. 10	Quadrupole gas analyzer spectrum of $\frac{\text{Mass}}{\text{Charge}}$ ratio versus partial pressure without Ar flow.	76
Figure 6. 11	Quadrupole gas analyzer spectrum of $\frac{\text{Mass}}{\text{Charge}}$ ratio versus partial pressure without Ar flow for a long time.....	77

ACKNOWLEDGEMENTS

This thesis would not have been possible without the support and guidance of my advisor Dr. Rama Venkat. I cannot thank him enough.

I am indebted to my parents for providing me the means to learn.

I would like to thank,

- a) Dr. Henry Selvaraj, Dr. Paulo Ginobbi for taking time and being in my committee.
- b) Dr. Clemens Heske for serving as the graduate college representative.
- c) Stanley Goldfarb for his invaluable suggestions and help.
- d) Dr. Allen L. Johnson and Dr. Robert J. Fairhurst for helping me with the XPS and SEM respectively.
- e) Dr. Robert A. Schill, Jr for his constructive comments and suggestions during this research.
- f) Brandon Blackstone for his help throughout the research
- g) Pavan Singaraju and Varun Jain for their support and helpful comments.

CHAPTER 1

INTRODUCTION

Neutron detection is important for applications in a wide range of fields such as home land security, power generation and in scientific experiments [1]. Neutrons are subatomic particles with no electrical charge making them difficult to detect. Hence neutron detection can only be achieved indirectly through its nuclear interaction with materials in which energetic charged particles such as alpha, α , can be created and detected [2]. The α particle interacts with certain semiconductors and gives rise to a number of electron-hole pairs proportional to its energy, which is directly related to the energy and flux of the neutrons. The generated electron-hole pairs can be detected either electrically as a current in the external circuit [3] or as emitted flux of photons if semiconductors are used [4].

^{10}B , an isotope of Boron, can be used as a nuclear reaction matrix material for the neutron capture along with a substrate of semiconductors like GaAs [2]. Alpha particle resulting from the neutron interaction with ^{10}B deposits its energy within a few tenths of nanometers of GaAs creating electron-hole pairs. In the traditional detectors based on electrical current output, either an external electric field or internal electric field arising from the depletion of doped semiconductors at the interface, is used to separate the electrons and holes.

These carriers result in an external current, which directly relates to the energy and flux density of incoming neutron [5].

The other possible approach to detecting the number of electron-hole pair generated is to detect the photon emission through band-to-band recombination which will result in photons of band gap energy of GaAs, which is 1.42eV. The number of photons emitted directly relates to the energy and flux density of incoming neutron. These photons can be easily detected using appropriate photo-detectors schemes using photomultiplier tubes.

In both the approaches, the thickness of ^{10}B is a critical parameter. If the thickness of the ^{10}B is large, neutron capture will be efficient, but, the α particle emitted at a location more than the mean free path of the alpha particle (10s of nm [6]) from the ^{10}B - GaAs interface, will be reabsorbed by ^{10}B and will be lost from detection in GaAs. If the ^{10}B is very thin (compared to mean free path of α in ^{10}B), then most of the α particles created will reach GaAs and result in electron-hole pairs, but the neutron capture in B^{10} will be inefficient. Thus, control of thickness of ^{10}B is very critical in building an optical and efficient neutron detector.

Thus, there is a need to deposit controlled thickness of ^{10}B on semiconductors such as GaAs. To coat a thin film of ^{10}B on a semiconductor, various deposition techniques can be employed and sputtering is one of them. Unfortunately, the ^{10}B in cylindrical disc form necessary for a typical sputtering system is very expensive. But, a hollow hemispherical ^{10}B -carbon alloy of inner diameter 2.5cm and outer diameter 4.755cm was available to us and hence a sputtering system had to be designed and built for a hemispherical target. Since vacuum components and parts were expensive and out of the financial range for the project, the design had to be accomplished with the parts and

components available to us in the laboratory. The focus of this thesis is the design, building and testing of sputtering system with a hollow hemispherical ^{10}B target.

1.1 Organization of the Thesis

In chapter 2, a literature review on neutron detectors is presented. In chapter 3, the physics of plasmas and sputtering and vacuum systems are presented. Also the details of the instruments used in thin film characterization and leak detection are presented in Chapter 3. In chapter 4, the paper design of the sputtering system using SOLIDWORKS 2006 and TRICOMP 6.0 SOFTWARES is presented along with the fabrication of the sputtering system. The experimental procedure employed for the operation of the sputtering system is also presented in chapter 4. Results and discussions are presented in chapter 5. Conclusions and recommendations for future work are presented in chapter 6.

CHAPTER 2

NEUTRON DETECTORS

2.1 Principle of Operation

Neutron detectors fall in to two categories: those suitable for detecting thermal neutrons (low energy) and those that directly detect and measure the energy of fast (high energy) neutrons. Boron 10 (^{10}B) absorbs the slow moving thermal neutron effectively and yields alpha (α) particles. If the α particles can be absorbed in a semiconductor to yield electron- hole pairs, then the electron- hole pairs can be detected and hence the presence of neutron particles.

When a low-energy neutron is captured by a ^{10}B nucleus, the products of the induced nuclear reaction are the lithium-7, usually in an excited state, and a helium nucleus (alpha particle) (Equations 2.1 and 2.2). Both of these species are born as positive ions with significant kinetic energy. When a neutron is absorbed by a ^{10}B atom, an alpha particle and a recoil Li-7 nucleus are produced that travel off in opposite directions. The movement of the alpha particle and Li-7 nucleus creates primary ion pairs in the gas. The size of the resulting pulse depends on whether the lithium nucleus is left in the ground state or an excited state. When the lithium nucleus is left in the ground state (about 6% of the time), the pulse is larger than if the nucleus were left in an excited state

(about 94% of the time) because the alpha particle and Li-7 nucleus have more kinetic energy (2.792MeV for the excited state vs. 2.310MeV for the ground state) with which to create ion pairs (Figure 2.1).

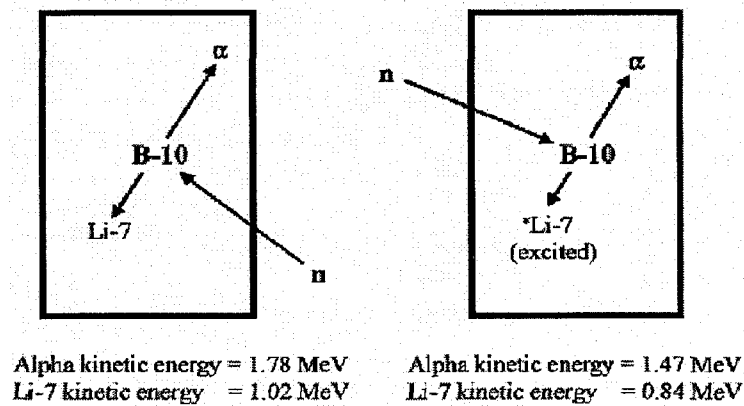
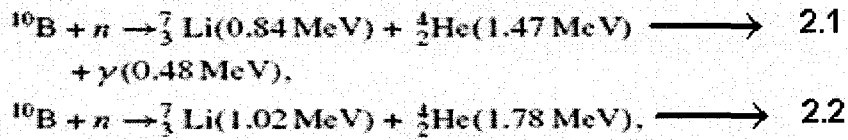


Figure 2. 1 A Schematic diagram of the reaction governing the boron based neutron detectors [7].

Semiconductor detectors coated with thin, neutron reactive films have been demonstrated as potentially useful devices for thermal neutron detection [7-10]. Semiconductor materials used for this application include bulk Si, GaAs, diamond, and amorphous Si. The semiconductor material substrate and the neutron-reactive film should have properties that assist in discriminating between neutron interaction events and γ -ray induced events. Si, diamond, and GaAs detectors have low γ -ray interaction probabilities due to their respective low atomic numbers.

A low operating voltage is a desirable attribute for semiconductor devices. Both Si and GaAs can be produced with high purity that the depletion voltage for a detector diode can be extremely low. Detectors fabricated from high-purity epitaxially grown GaAs layers demonstrate very good results under zero bias conditions due to the existence of the electric field in the depletion layer even under equilibrium conditions [11].

2.2 Device Structure

Planar Semiconductor detectors consist of a layer of neutron converter material coated on the device surface (Figure 2.2). ^{10}B is frequently used as a thermal neutron converter material. The thermal neutron ^{10}B reaction produces charged particles: alpha particles (1.47MeV) and ^7Li (0.84MeV) [7]. These charged particles enter the semiconductor detector material and create electrons and holes for generation of electrical signals. However, these charged particles travel inside the converter materials only for a short distance.

The alpha particle travel distances in different materials are calculated by finding the mean range of travel distance in which the intensity of alpha particles drops by a half. The range of (1.47MeV) α particle in boron 10 is $\sim 3.3\mu\text{m}$ [18]. Thus, if the boron layer is very thick, the charged particles will be absorbed in the ^{10}B layer itself before they reach the semiconductor material. But, the converter material needs to be sufficiently thick to capture most of the incoming thermal neutrons. Thus, the thickness of ^{10}B should be carefully chosen to maximize the neutron absorptions in ^{10}B and at the same time allow maximum absorption of alpha (α) particles in the semiconductor.

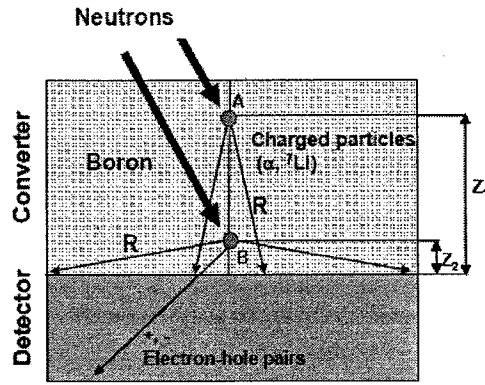


Figure 2. 2 A Schematic diagram showing the location of various nuclear interactions in a solid state neutron detector [7].

A schematic diagram of the planar neutron detector is shown in Figure 2.2 to explain the limitation of active converter material thickness. The charged particles from the thermal neutron ^{10}B reaction emitted from point A at distance Z_1 from the detector have a low probability to reach the semiconductor detector. Only the forward directed particles emitted can reach the detector and produce signals in the semiconductor. The rest of the particles are stopped in the converter. Clearly, the probability of signal generation for particles emitted from point B, at $Z_2 < Z_1 < R$, is much higher than for the ones from point A. Thus, only a limited converter thickness is effective for the detection. The upper limit of the detector thickness can also be evaluated by the mean travel range of alpha particles for different materials. For α (1.47MeV) in silicon, the mean free path is $\sim 5.3\mu\text{m}$.

2.2.1 Boron Deposition

The ability to deposit conformal and uniform coating of ^{10}B is one of the key steps to a successful fabrication of a neutron semiconductor detector. Since alpha particles are

generated in the $^{10}\text{B} (n, \alpha)$ reaction, any air gap between the semiconductor and the boron layer will decrease the detector sensitivity as the alpha particle will be lost to the reactions in the air gap. Thus, high-aspect-ratio is required. Common methods for boron deposition are electron beam (e-beam) evaporation, sputtering, and chemical vapor deposition. Each of these techniques is described briefly in the following sections.

2.2.1.1 E-beam evaporation

E-beam evaporation of boron is the most commonly used method to deposit boron because of its simplicity in the requirement of the boron source, which is typically solid source. Extensive investigations were performed to optimize the evaporation of boron [18]. Since boron has high melting and sublimation points of 2076°C and 2550°C , respectively, electron beam, rather than resistive heating, is required to supply enough energy for vaporization by directly coupling the e-beam energy to the bonds in the solid ^{10}B . Boron source targets with low purity (90% or less) or uneven heating of the boron target will cause non-uniform evaporation rates and “spitting” of materials from the evaporation target, which can result in non-conformal and spatially non uniform ^{10}B films [16].

2.2.1.2 Sputtering

Sputtering is another method to deposit boron onto high-aspect-ratio structures. Since the sputtering action of the boron targets would generate boron clusters in randomized directions, the as-deposited boron layer is expected to be more conformal to the geometry of the substrates. However, as boron is a poor conductor charging of the target during sputtering will occur. Therefore, a pure boron sputtering target will usually yield low deposition rates unless the boron is coated as a thin layer on a conductor [19].

Another way to avoid charging of the target is to use RF or pulsed dc sputtering. Yet another way to avoid charging is to use semi-conducting boron carbide (B_4C) or doped boron is often used as the sputtering target to deposit materials with boron 10 isotopes.

2.2.1.3 Chemical Vapor Deposition

Chemical vapor deposition (CVD) is a well-known deposition technique to produce conformal coverage of materials on high aspect- ratio structures. Two of the common precursors for CVD of boron are diborane (B_2H_6) and decaborane ($B_{10}H_{14}$). Diborane exists as a gas at room temperature. Thermal CVD with diborane has been successfully applied to grow boron films at 600-1000°C [19]. Though the gaseous form of this chemical allows the ease of transport to the reactor, its high toxicity often requires expensive safety precautions, such as the installation of gas cabinets and relatively expensive production of chemical containing ^{10}B . Decaborane has become one of the preferred precursors for boron deposition due to its advantageous physical properties. First, high purity decaborane can be easily obtained with sublimation purification processes (Sublimation temperature $\sim 70^\circ C$). Second, even though decaborane is toxic, since the decaborane is in solid form at room temperature, the materials can be easily contained and handled.

Furthermore, decaborane has a lower thermal decomposition temperature (~ 200 - $400^\circ C$) for thin film deposition [20]. Since decaborane is in solid form at room temperature, it needs to be sublimed at $70^\circ C$ into its gas form for delivery to the reactor. Similar to other non-gaseous precursors, precise control of non-gaseous form materials would require special heated mass flow controllers and manometer set up to control the dynamics of materials deposition.

2.2.2 Theoretical Considerations and Detector Design

2.2.2.1 ^{10}B Film Coatings and Efficiency

The microscopic thermal neutron absorption cross section increases with decreasing neutron energy; thus, the cross section dependence is proportional to the inverse of the neutron velocity ($1/v$) in much of the energy range [12]. Neutrons may interact anywhere within the reactive film, and the reaction products lose energy as they move through the neutron reactive film. Usually, ^{10}B absorption cross section is obtained by subtracting a relatively small known scattering cross section from the measured total cross section. Self-absorption of the reaction product reduces the energy transferred to the semiconductor detector, thus limits the maximum film thickness that can be deposited over the device's blocking contact. The measured voltage signal is directly proportional to the number of electron-hole pairs excited within the semiconductor.

Reaction products that deposit most or all of their energy in the detector will produce much larger voltage signals than those reaction products that lose most of their energy before reaching the detector. The energy absorbed in the detector is simply the original particle energy minus the combined energy lost in the boron film and detector contact during transit [9, 11].

2.2.2.2 Diode Structures

McGregor et al., fabricated ^{10}B coated GaAs neutron detectors. GaAs devices coated with films of 98% enriched high-purity GaAs. For the high-purity epitaxial GaAs devices, the difference between the work functions of the blocking contacts and the v-type high-purity GaAs active region produced an internal potential difference at the ^{10}B - GaAs interface [15]. This built-in potential produces an internal electric field, which,

thereby, depletes sufficient portion of the v-type GaAs region. Depleted GaAs has an internal electric field and this electric field allows the drift of electrons and holes in the opposite direction, which results in an electric current proportional to the neutron energy. Therefore, an external voltage bias is not required to operate the devices (Figure 2.3). But an external voltage source is necessary to operate the supporting readout electronics.

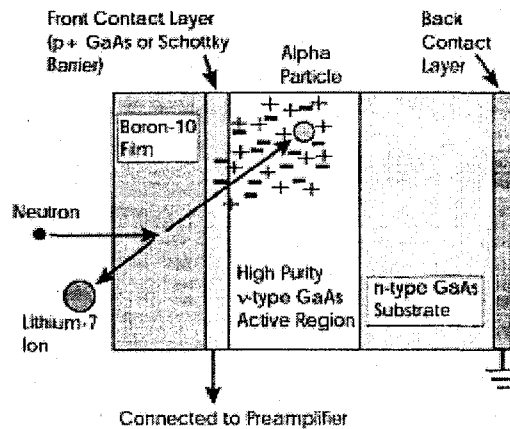


Figure 2. 3 A Schematic diagram of the device structure [15].

For these devices to become viable thermal neutron beam monitors they must be able to withstand the harsh environment produced from a variety of neutron sources, such as a nuclear reactor, a solid source, or a generator. In other words, materials such as GaAs used in the detector should be made radiation hard.

2.3 Monte Carlo N-Particle Simulation (Theoretical analysis)

The development of neutron detectors makes extensive use of the predictions of detector response through the use of Monte Carlo technique. The general Monte Carlo code was developed at Los Alamos National Laboratory, Monte Carlo N-Particle

(MCNP). It was originally intended for neutrons, but has been extended to include gamma rays and electrons as well. Se-Hwan Park et al., used MCNP to calculate neutron efficiency of a kapton foil in a gas electron multiplier. The neutron converters of the B compound and LiF were included in their calculation. The thermal neutron detection efficiencies of the converter foil were calculated as a function of the converter thickness. The thermal neutron was assumed to be incident perpendicular to the converter. For a given thickness of the neutron converter, the converter was assumed to be composed of slices of the same thickness. The probability of the neutron conversion into the charged ions in each slice was obtained with MCNP. The calculated thermal neutron efficiency as function of the converter thickness is as shown in Figure 2.4.

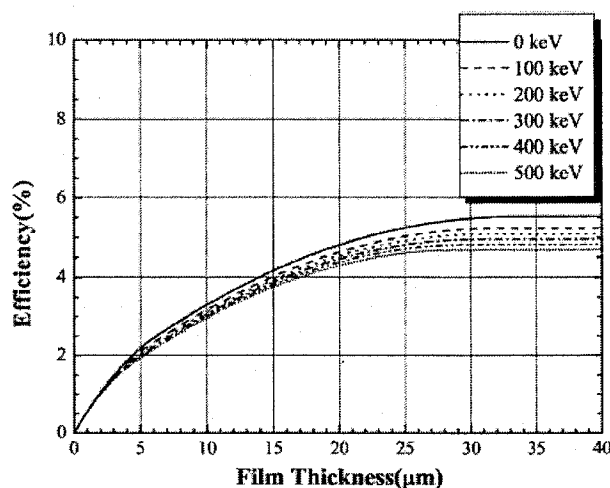


Figure 2. 4 A plot of Efficiency Vs Film thickness from MCNP [22].

Figure 2.4 shows a plot of thermal neutron efficiency as a function of cutoff of charged particle detection. The calculation was done for ${}^6\text{LiF}$ converter too. It can be seen as the cutoff energy becomes higher and higher, the neutron detection efficiency of the ${}^{10}\text{B}$ converter decreases more rapidly than the case of the ${}^6\text{LiF}$ converter [22].

2.4 Device/Detector Results [15]

McGregor et al., investigated various ^{10}B /GaAs based neutron detectors from six different diode configurations as tabulated in Table 2.1

Table 2. 1 Various diode configurations studied by McGregor et al., [15].

Sample Number	Diode Type	Boron-10 Thickness	Blocking Contact	v-type GaAs ($n \approx 3 \times 10^{14}/\text{cm}^3$)	Intermediate Layer	Substrate
3241	<i>p-i-n</i>	5000 Å	<i>p+</i> GaAs ($2 \times 10^{19}/\text{cm}^3$) 2000 Å	5 μm thick	None	<i>n</i> -type GaAs
3242	<i>p-i-n</i>	6500 Å	<i>p+</i> GaAs ($2 \times 10^{19}/\text{cm}^3$) 2000 Å	2 μm thick	None	<i>n</i> -type GaAs
3243	<i>p-i-n</i>	7200 Å	<i>p+</i> GaAs ($2 \times 10^{19}/\text{cm}^3$) 2000 Å	5 μm thick	None	<i>n</i> -type GaAs
3246	<i>p-i-n</i>	5000 Å	<i>p+</i> GaAs ($2 \times 10^{19}/\text{cm}^3$) 2000 Å	1 μm thick	None	<i>n</i> -type GaAs
3247	<i>p-i-n</i>	5000 Å	<i>p+</i> GaAs ($2 \times 10^{19}/\text{cm}^3$) 2000 Å	2 μm thick	<i>n</i> -type $\text{Al}_x\text{Ga}_{1-x}\text{As}$ ($5 \times 10^{15}/\text{cm}^3$) 2500 Å	<i>n</i> -type GaAs
3278	Schottky Diode	6500 Å	Au Schottky Contact 200 Å	5 μm thick	None	<i>n</i> -type GaAs

Self biased devices (Figure 2.3) from all the six samples demonstrated a similar counting efficiency to the expected efficiency indicating that the v-type regions need to be very thick to operate as viable, low power neutron detectors. The best spectral response was observed from sample 3241 and best counting efficiency from sample 3243. The worst spectral performance was observed in sample 3242, although the counting efficiency matched the theoretical efficiency values. The 3278 Schottky barrier devices did not perform well as they demonstrated higher electronic noise. Devices should have thicker ^{10}B films to increase neutron detection efficiency closer to the theoretical maximum. The self biased design offers a straight forward method to produce low cost, lightweight low power neutron detectors [15].

CHAPTER 3

PLASMA AND SPUTTERING

In this chapter, the physics of plasmas and sputtering are discussed in detail. Details of various types of plasmas and sputtering are also presented.

3.1 Plasma

Plasma is the fourth state of matter (Figure 3.1). Plasma is a gaseous state of matter containing an equal number of positively and negatively charged particles per unit volume in addition to neutral atoms. Plasma is created by adding energy to gas. Simplest way to create plasma is by heating the gas. A gas can be converted in to thermal plasma if it is heated to a very high temperature. Gases at room temperature contain small concentration of independent charged particles. In order to produce high concentration of charged particles to create thermal plasma, temperature of the gas has to be raised from 4000 °K to 20,000 °K. At these high temperatures, the free electrons within the gas have high enough kinetic energies to ionize sufficient fraction of the gas-atoms to produce a stable plasma state. Due to the impracticality of achieving such high temperatures as 4000 °K other ways are employed to achieve plasma.

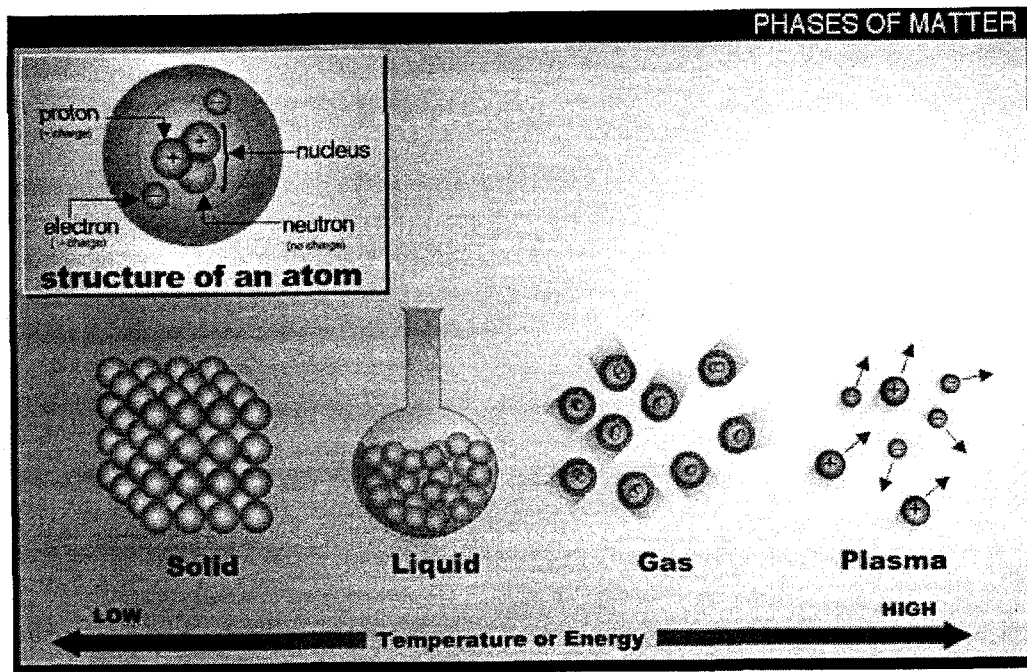


Figure 3. 1 A schematic representation of the four states of matter [17].

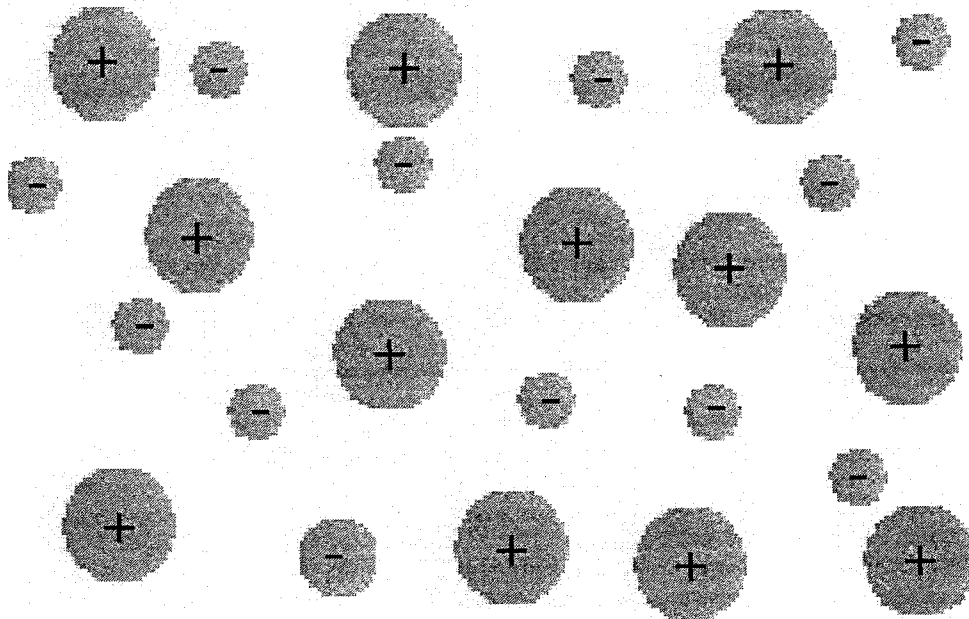


Figure 3. 2 A figure showing schematic diagram of plasma [25].

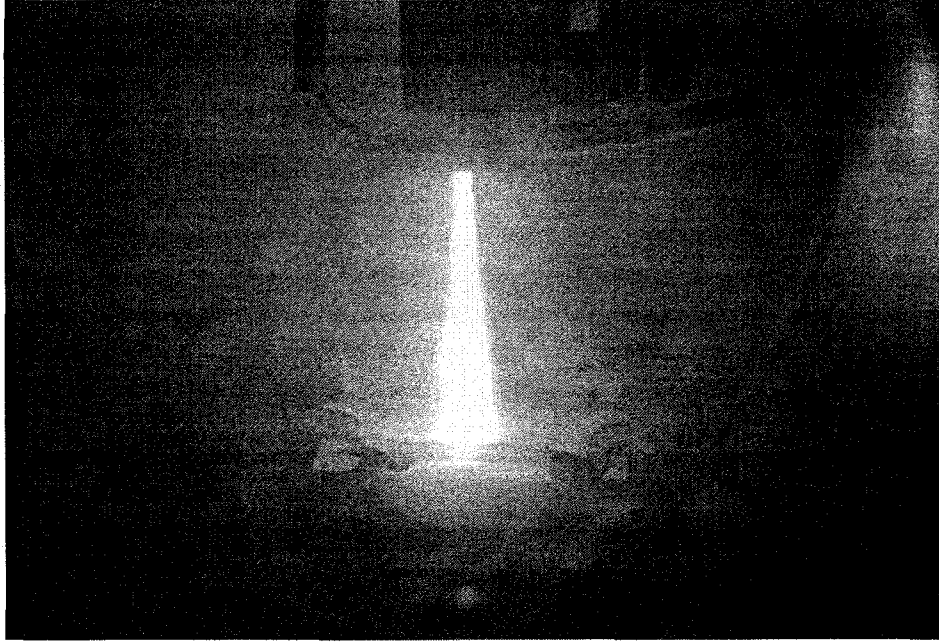


Figure 3. 3 A photograph showing thermal plasma [30].

One way of initiating plasma is by touching together two electrodes and then separating them while applying a large potential difference between electrodes. This, in turn, ionizes some of the air molecules causing the gas to be conductive [24]. This allows a current to flow between the electrodes, which is necessary to sustain the intensely heated arc discharge plasma. This type of plasma is called arc discharge plasma and is used for welding purposes. Another type of plasma called glow discharge plasma is employed in the semiconductor industry. They are weakly ionized plasmas and can be created by adding energy from electric and magnetic fields to the gas. This allows only the charged-particles in the plasma to gain energy. And by gaining sufficient amount of energy in this way, free electrons are not only able to ionize the gas atoms and produce plasma, but also allows to create reactive species [23].

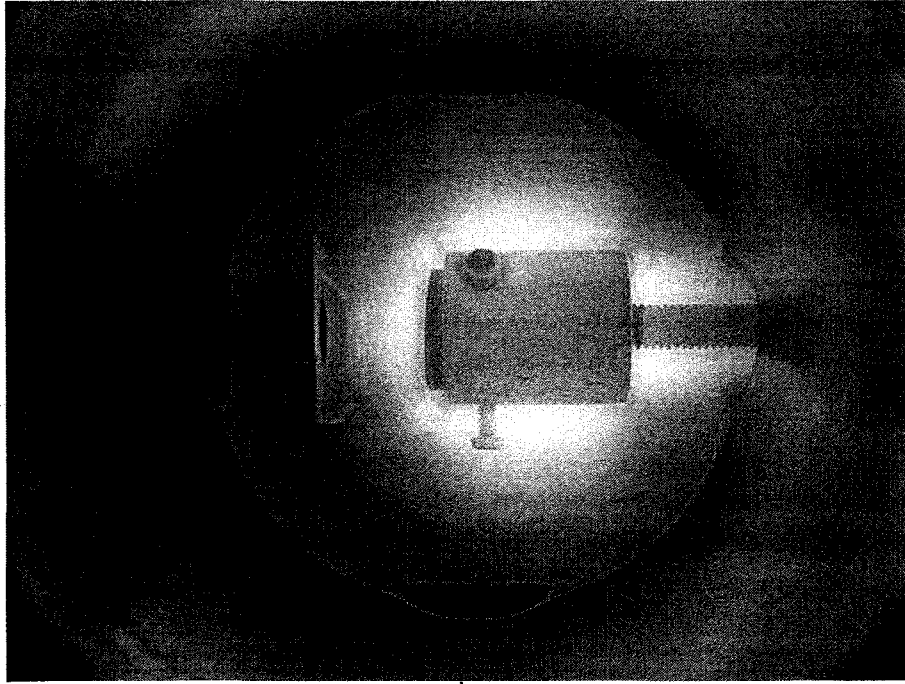


Figure 3. 4 A figure showing glow discharge plasma [25].

Since glow discharge plasmas are widely used in the semiconductor industry, they will be discussed in the following sections.

3.1.1 Introduction to Glow Discharges

A glow discharge is a self sustaining, weakly ionized plasma, that emits light. Neon light is an excellent example of glow discharge plasma. Different variants to glow discharge plasmas are direct current (DC) glow discharge, capacitively coupled radio-frequency (cc RF) glow discharge, alternating current (AC) glow discharge, pulsed glow discharge, magnetron discharge, inductively coupled discharge, microwave induced plasmas. Direct current (DC) glow discharge and radio-frequency (cc RF) glow discharge are discussed in detail due to their wide spread use in IC-processing.

3.1.1.1 Direct current (DC) glow discharge

The dc-diode system consists of a glass tube from which air has been evacuated. It is then, re-filled with a specific gaseous species at low pressure. Within the tube are two electrodes, the positively charged anode and the negatively charged cathode. A dc-potential difference is applied between them which results in a constant current [23].

Creation of DC Glow Discharges

A glass tube (as shown in Figure 3.5) is taken and is filled with argon (Ar) gas at a pressure of 1torr. The distance between electrodes in the glass tube is 15cm. A 1.5kV DC potential difference is applied between them. At the onset of the potential difference, no current flows in the circuit because all the Ar gas atoms are neutral and there are no charged particles in the gas. The applied 1.5kV is fully dropped between the two electrodes. If a free electron enters the tube, it will be accelerated by the electric field that exists between the electrodes. Usually this electron is created by a passing cosmic ray. The mean free path of an electron in the gas at 1torr is 0.0122cm.

Figure 3.5 shows the negative and positive densities present in the DC glow discharge along the length of the tube, the voltage as a function of position in a DC glow discharge along the length of the tube, and electric field strength in the dc glow discharge along the length of the tube [23].

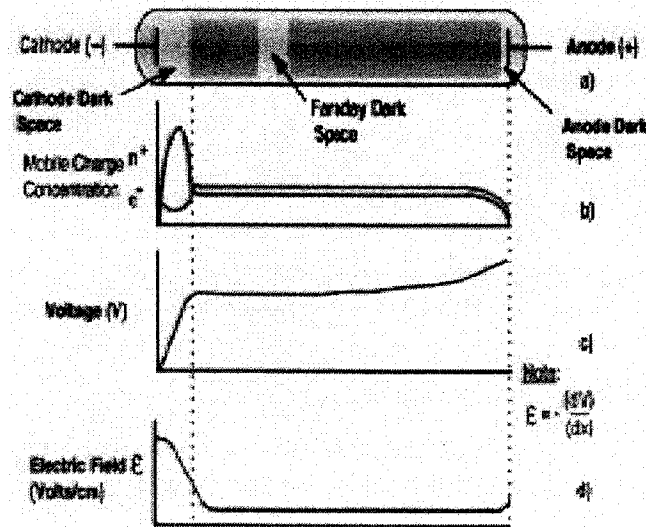


Figure 3. 5 A figure showing schematic drawing of a dc glow discharge established in a glass tubes containing a gas under reduced pressure [23].

Events associated with electron-gas collisions in a glow discharge are [23]:

1. Elastic Collision : No energy is lost by the electron due to collision
2. Inelastic Collision Type I: Electron impact ionization causes an electron in a gaseous atom to escape from its atomic structure thereby creating a free electron and an ion.
3. Inelastic Collision Type II: In this type, electron is excited to a higher energy level. When this electron relaxes back to its original energy level, it emits photon which is responsible for the glow discharge.

Most of the collisions in glow discharge are elastic. They occur because the mass of the electron is much smaller compared to the mass of the atom. The mean free path of an electron for inelastic collision is about 0.122cm. If this is the minimum, then there must be significant electron path lengths of 0.5 – 1.0cm. When a free electron travels 1cm in

the 100V/cm electric field, it would have picked up a kinetic energy of 100eV. With this kinetic energy, the free electron can transfer enough energy to excite an electron in an argon gas atom. If the transferred energy is less than the ionization potential, one of the orbital electrons of an Ar atom will be excited to a higher energy state and then, relax back to its original energy state by emitting a photon. Such excitation events are the source of the characteristic glow of the discharge. Glow discharges of different gases emit light of different colors due to difference in atomic energy transitions among various gaseous species. If the transferred energy is greater than the ionization potential, then a second free electron and a positive ion are created. Both the free electrons (confined electron and electron created by impact ionization) will get accelerated and result in an avalanching or cascading type effect [23]. This results in a large number of electrons.

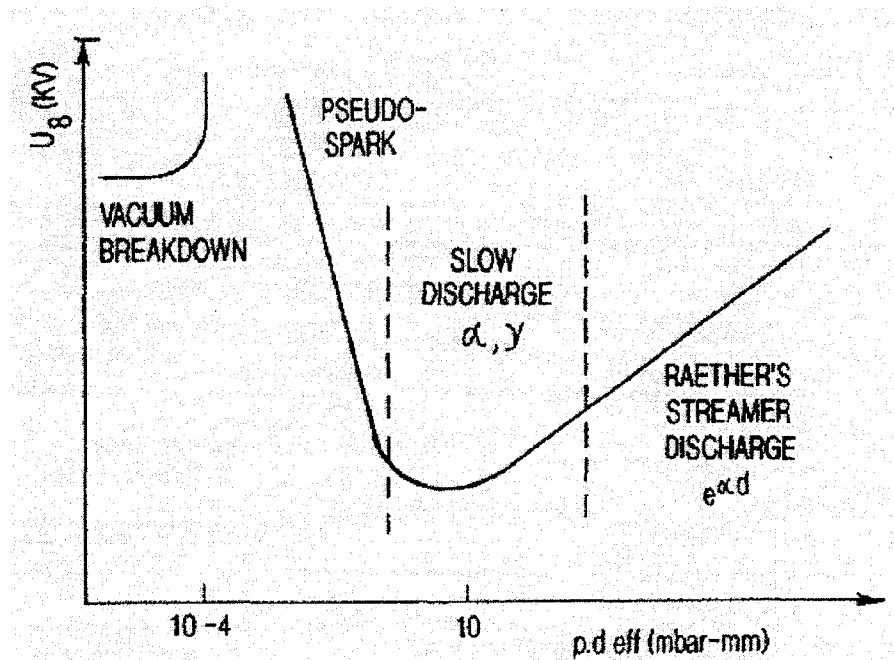


Figure 3. 6 A figure showing the paschen curve [23].

Figure 3.6 shows the break down voltage required to initiate the discharge, as a function of the product of the gas-pressure (P) and the electrode spacing (d). This is called a paschen curve. When the condition of gas break down is reached, current flows in the external circuit as a result of availability of free electrons. Ionization event occurs closer to the anode. Unless there is a mechanism available for generating additional free electrons, the current will quickly increase to a maximum value, then decay to zero. When there are sufficient amount of electrons to sustain the discharge it is said to be self sustained.

Events that occur when electrons collide with gas atoms and molecules are [23]:

1. Atomic Excitation
2. Atomic Ionization

Events resulting from Electron/Gas-atom collisions are [23]:

1. Molecular Excitation
2. Molecular Ionization
3. Dissociation and Ionization

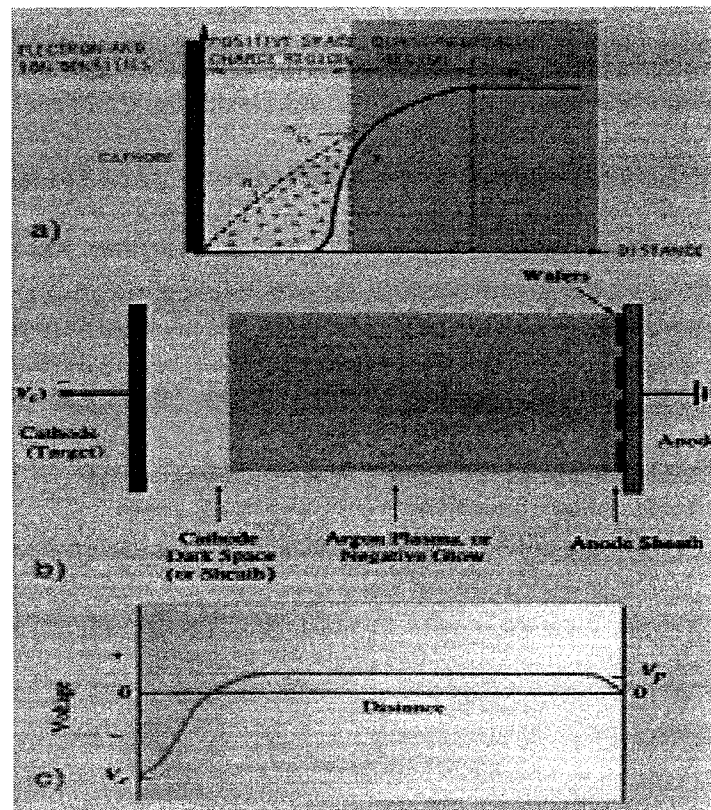


Figure 3. 7 A schematic figure showing (a) charge density of ions and electrons (b) plasma and dark regions and (c) electrostatic potential as a function of location between the anode and the cathode [23].

- Avalanche Breakdown occurs when the electrode voltage exceeds the product of gas pressure and between anode and cathode spacing.
- A dark space exists between cathode and the glow region, where there is no plasma.
- Excessive positive ion present in the dark space region creates an electric field between the edge of the dark space and cathode.
- In the dark space, ions get accelerated and gain energy.

Figure 3.7 shows the distribution of charge near the cathode. Positive ions of the discharge are present in higher density near the cathode, which results in a localized positive charge in that place. Therefore, any electrons near the cathode are accelerated away from it due to their negative charge and small mass. Heavy ions are accelerated towards the cathode slowly. It takes longer time for the ions to cross the dark space than the electrons. Therefore, the concentration of ions in dark space is greater than that of electrons. Presence of space charge greatly increases the electric fields near the cathode which implies that the electric field in the rest of the tube is rather weak. Most of the voltage dropped between the anode and the cathode is across the dark space. Hence charged particles experience their largest acceleration in this region. Usually, negligible amount of light is emitted from the dark space due to the following reasons. Since the electrons in the dark space are accelerated due to the presence of strong electric fields and travel through the space quickly, the electron density at any instant in the dark space is reduced drastically. The small number of electrons present in the dark space gain high energies from the electric field. When these electrons collide with the gas atoms in the dark space, ionization rather than excitation results. Due to which fewer light generating electron-atom collisions occur in the dark space than in negative and positive glow regions [23].

Cathode emits electrons when it is struck by ions. Upon entering the dark space these secondary electrons are accelerated towards the anode. They gain high enough energy during the acceleration to cause ionizing and light emitting collisions with the gas atoms. Edge of the glow region provides an indication of the starting location of such events. If the pressure in the tube is reduced, then the probability of such collisions is greatly

reduced and the dark space gets wider. If the pressure gets too low, then the dark space extends fully between the two electrodes and glow gets extinguished. Sufficient amount of secondary electrons has to be emitted to keep the discharge self sustaining and these electrons must undergo adequate ion-producing collisions with the gas in the tube. These ions must be created in the dark space and the glow regions to generate sufficient secondary electrons to sustain the discharge [23].

3.1.1.2 Radio Frequency (RF) glow discharge

DC diode system cannot sustain glow discharge if the electrodes are covered by insulators. Electrons are stripped off from the negatively biased cathode each time a bombarding positive ion is neutralized. If the cathode material is a good conductor, then such electrons are replaced by electrical conduction and cathode surface will maintain the negative potential required to sustain the discharge. If the cathode surface material is an insulator, then the electrons lost from the cathode surface are not replenished because of the spatial discontinuity in the electrical conduction. Therefore, the front surface of the cathode accumulates positive charge with the ion bombardment, thereby causing a potential difference between the cathode and the anode to decrease. When the potential drops below a certain value the glow discharge extinguishes. Radio frequency glow discharge technique was developed to replenish the electrons lost to ion neutralization at the front surface of an insulating cathode. Glow discharge based on the application of small ac voltage across the electrodes is known as RF glow discharges. Figure 3.8 shows the static DC electrode potential as a function of position across the tube. RF-signal is superimposed on a dc-signal. The plasma is conductive so the voltage drop across the

glow discharge is less. Huge voltage drops exist between plasma and the electrodes due to electron depletion. Usually, RF-glow discharges are operated at 13.56MHz [23].

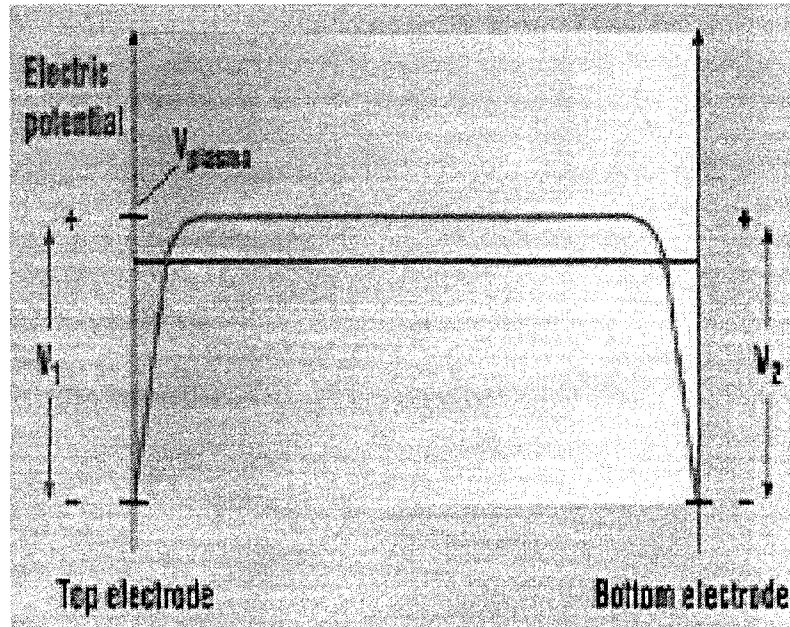


Figure 3. 8 A Schematic figure showing electrostatic potential versus distance between the two electrodes [23].

Similarities and differences between RF and DC plasma are presented in Table 3.1

Table 3. 1 A comparison of RF and DC plasmas

SIMILARITIES	
Characteristic	Result
Electrical current	principally by ions bombarding the sample
Potential distribution	similar in RF and DC
Electric fields	similar in RF and DC
Density of ground state	similar in RF and DC
Ion densities	similar in RF and DC
Ar intensities	similar in RF and DC
Net sputtering rate	similar in RF and DC
Sputtered species	similar in RF and DC
DIFFERENCES	
Electron impact ionization	more efficient in RF than DC
Plasma potential	lower in RF than DC
Ion density	drops more slowly away from the sample in RF than DC
Plasma cell	more filled with argon ions than DC
Excitation	more efficient in RF than DC
Population of excited levels	higher in RF than DC

RF plasma is preferred over the dc plasma because of the following reasons [24]:

- Wider range of operating parameters
- More stable plasma
- Less affected by surface oxides
- Greater sputtering depth.

3.2 Sputtering

The sputtering phenomenon was first observed by W.R.GROVE after he observed a cathode material transfer onto a polished silver plate during a gaseous discharge investigation [26]. The word “sputter” means to dislodge atoms from the surface of the material by collision with high energy particles. By definition, sputtering is the mechanism in which atoms are ejected from the surface of a material when it is struck by sufficiently energetic particles [23].

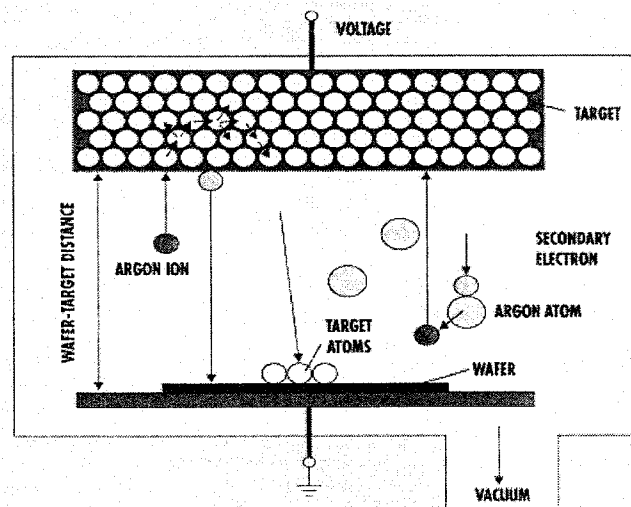


Figure 3. 9 A schematic diagram illustrating the steps in sputtering process [31].

3.2.1 Physics of Sputtering

The four important stages of a sputter process (Figure 3.9) are : (1) ions are generated and directed towards the target, (2) these ions sputter atoms from the target, (3) ejected atoms are transported to the substrate and (4) the sputtered atoms condense and form a thin film on the substrate [23]. When a solid surface is bombarded by atoms, ions or molecules at moderate energies, the following physical process happen: (1) Some fraction of the energy of the impinging ions is transferred to the solid as heat or lattice damage, (2) Another fraction causes the atoms from the surface to be dislodged and ejected into the gas phase [23].

Usually an inert gas such as Argon is injected in to a vacuum chamber consisting of the target (cathode) and the substrate (anode) which is separated by 5 to 10cm (Figure 3.10). Typically a dc voltage of 240V is applied between the anode and the cathode. In these systems, the discharge species is the plasma, which consists of positive ions, electrons and neutral species in a quasi neutral electrical state. The details and the physics of plasma were discussed in section 3.1. Magnets are often placed behind the target surface. The magnetic fields from the magnet help to confine the dense plasma near the target surface and increase the consequent ion bombardment of the target and ion efficiency. Once the plasma is formed, positively charged gas ions start bombarding the negatively biased target and the target atoms are dislodged through the energy transfer from the striking gas ions. Then the target atoms are ejected towards the substrate with sufficient kinetic energy will land on it [23].

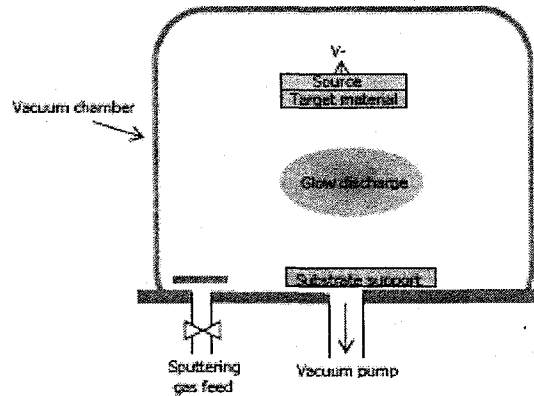


Figure 3. 10 A picture showing the sputter environment [28].

Since plasma is involved in this sputtering, this kind of sputtering is also called as Plasma sputtering. Plasma sputtering can be divided into three sub categories based on the means of plasma discharge. They are: Direct current (DC), Alternating current (AC) and Radio Frequency (RF). DC and AC are implemented to sputter conducting materials whereas RF is used sputter insulating and semi conducting materials [27]. Details of magnetron sputtering are discussed in the subsequent sections.

3.2.2 Magnetron Sputtering

The basic feature of a magnetron discharge is the confinement of the plasma in front of the target (cathode). This is achieved by a combination of electric and magnetic fields [29]. The magnetic field strength is adjusted in such a way that the electrons are significantly influenced by the magnetic field while the ions are not. The electrons perform cycloidal orbits in the crossed electric and magnetic fields, leading to very high ionization efficiency. Therefore, magnetron discharges can be sustained at much lower pressures or higher current densities than the glow discharges without magnetic assistance. In standard sputtering processes, there are usually two modes of powering the

magnetron sputtering system. These two modes are direct current (DC) magnetron sputtering or by radio frequency (RF) magnetron sputtering (Figure 3.11). In DC magnetron sputtering, a direct voltage is applied between the cathode and anode. This method works well with conductive targets. The second method involves the use of a radio frequency source with a typical frequency of around 13.56MHz. The magnetic field confines the electrons in front of the target in a torus-like plasma region which causes a non-uniform erosion of the target (Figure 3.12). The external discharge parameters such as working pressure, discharge power, design of the magnetic field and the excitation mode (DC or RF) influence the potential distribution and hence the particle energies.

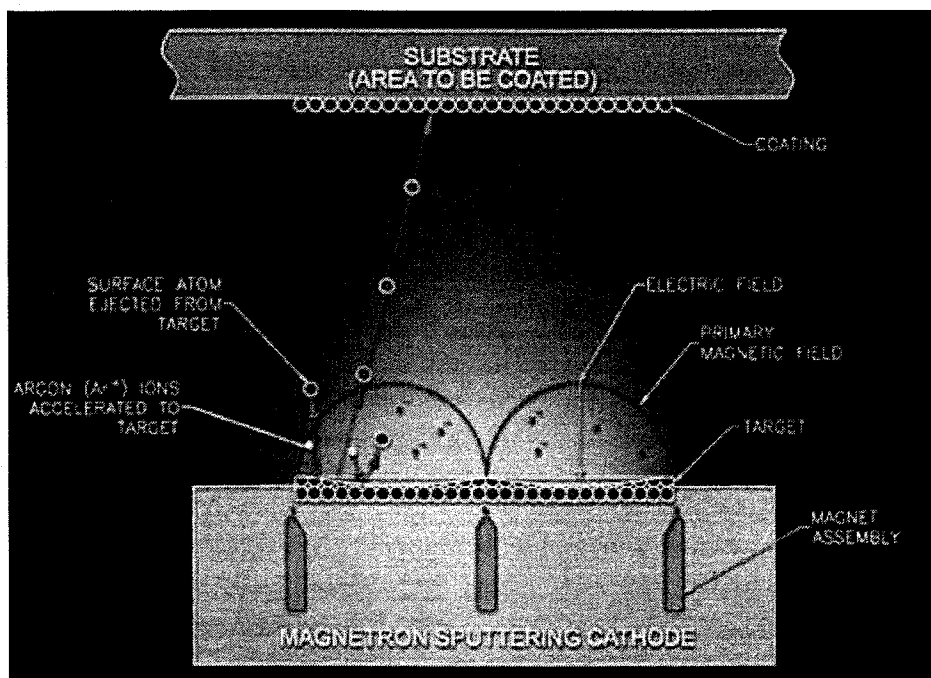


Figure 3. 11 A schematic picture illustrating the Magnetron sputtering process [32].

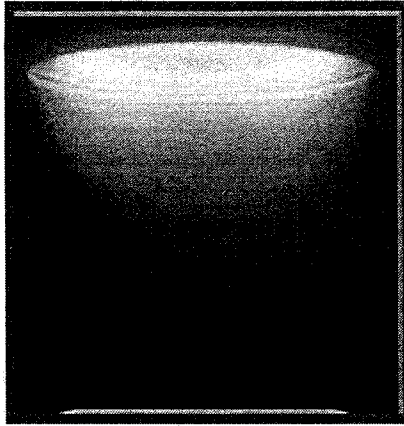


Figure 3. 12 A photograph showing the electron confinement which causes a non-uniform erosion of the target in magnetron sputtering [32].

Most of the sputtering occurs from a ring shaped region of the target immediately beneath the intense plasma ring in a Magnetron sputtering. Due to this type of non-uniform erosion of the target, the following problems arises

- Deposition rate across the substrate is less uniform.
- Target utilization is less uniform i.e. the target erodes in ring region and not elsewhere. Therefore, the target material must be replaced periodically.
- On regions of target surface away from the ring region, there can be a net build up of sputter deposited film, some of which adhere poorly to the target which may peel resulting in particle contamination in the sputter chamber [23].

The problem of non uniformity of sputtered film can be resolved in the following ways. First, the size of the target and the distance between the target and substrate is optimized to give uniformity. Secondly, permanent magnet behind the target is replaced with a movable magnet array [23].

CHAPTER 4

VACUUM SYSTEMS AND INSTRUMENTS USED IN THIN FILM

CHARACTERIZATION AND LEAK DETECTION

In this chapter, the necessary background details of the sub components of the sputtering system are provided. The sub components covered are vacuum systems, vacuum gauges, targets, the sputter head and the voltage pulse generator. Where, the appropriate physics of operation of the subcomponents are presented. Also the working of the instruments used in Thin Film characterization and leak detection are discussed.

4.1 Vacuum Systems

Thin Film deposition of electronic materials is done under vacuum conditions for various reasons. The primary reasons are: to increase the mean free path for deposited atoms, to provide clean environment, to eliminate the presence of gases that would react with the deposited material, and reduce the vapor pressure of deposited material which, in turn, lowers the evaporation temperature of deposited material. Vacuum is defined as an empty space or a space devoid of matter. In practice, a vacuum is created by eliminating atmospheric gases from a chamber and it's highly impossible to eliminate all gaseous atoms and molecules from any chamber or vessel. Also the level of vacuum needed depends on the process and application. Vacuum can be divided in to four main

categories: 1. low vacuum: (10^5 to 10^3 Pa) or (760 to 25torr), 2. medium vacuum: (10^3 to 10^{-1} Pa) or (25 to 0.75mtorr), 3. high vacuum: (10^{-1} to 10^{-4} Pa) or (10^{-3} to 10^{-7} torr), 4. ultra high vacuum: (10^{-4} to 10^{-7} Pa) or (10^{-7} to 10^{-12} torr) [4]. Most of the thin film deposition processes in the electronic industry are carried out under medium and high vacuum conditions.

Gases found in vacuum system are due to leaks in the chamber, desorption of moisture from the chamber walls, substrate holder and target materials and components and re-evaporation of other materials from the chamber walls. Sometimes virtual leakage may occur from the joints between any two materials or parts in a vacuum system. Joints vary in the amount of leakage and cost of implementation. Quality of vacuum required dictates the type of joints used. Evaporation from chamber walls are due to absorbed water, particulate matter and gases during their manufacture and every time the chamber is exposed to the atmosphere. These contaminants results in degradation of vacuum quality [34].

4.1.1 Vacuum Pumping Mechanisms

Based on the level of vacuum, the vacuum pumps can be divided in to two classes: Roughing pumps (760torr to 10^{-3} torr) and High Vacuum (less than 10^{-3} torr) Pumps can also be classified according to their pumping mechanisms. In the following sections, two pumps, a mechanical pump belonging to the first class and a turbomolecular pump belonging to the second class are reviewed. The discussion is limited to these two pumps as these are the two pumps used in this work.

4.1.1.1 Mechanical Pumps/Roughing Pumps

As the name implies these pumps are used to achieve a rough or low vacuum. Though they are capable of very high pumping rates, they have limited maximum obtainable vacuum. Common roughing pumps include oil sealed rotary vane, cryogenic absorption pump, roots blower, rotary piston and dry mechanical pumps. The most common rotary pump is oil sealed rotary vane and is used in our sputtering system. These pumps consist of a set of vanes embedded in a shaft. As this shaft is rotated by an external motor, gases in the large cavity of the pump is compressed and expelled through the exhaust. This compression produces a vacuum in the cavity which is, then, presented to the inlet to fill the vacuum in the pump with gas molecules from the chamber and, this gas is, then, compressed and expelled through the exhaust as the shaft rotation continues. (Figure 4.1) Thus the gases in the vacuum chamber are compressed and expelled out of the system. The cavity in these mechanical pumps is filled with oil, which provides lubrication, cooling, and a seal between the spring-loaded vanes (Figure 4.1) and the walls of the pump. The main limitation of these pumps is the maximum obtainable vacuum due back streaming of oil vapors in to the vacuum system. Hence a second class of pumps, High vacuum pumps is used to achieve high vacuum. These High vacuum pumps have lower pumping rate than roughing pumps but they can attain very high vacuum conditions. High vacuum pumps are used in combination with roughing pumps. High vacuum pump draws gases from the chamber, while roughing pump draws gases from the high vacuum pump [34, 35].

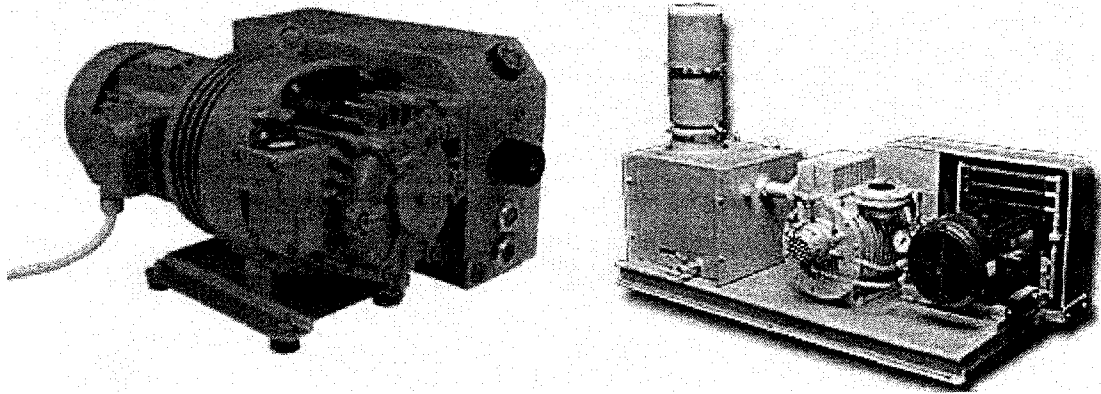


Figure 4. 1 Photographs of (a) Oil sealed rotary vane pump, (b) a cross sectional view showing the vanes [36].

4.1.1.2 Turbomolecular Pumps

Oil diffusion, Turbomolecular pumps (Figure 4.2), titanium sublimation, and ion pumps belong to the class of High-vacuum pumps. Turbomolecular pump that is used in our system uses a series of blades, which behave in a manner that is similar to jet engine turbine. The rotors are accelerated to very high speed of about 56 krpm by a motor in the pump assembly. These blades impart momentum to gas molecules in the vacuum chamber. The molecules are imparted momentum away from the chamber in to the inlet of a mechanical pump. These pumps are small and require a mechanical or dry pump to provide backing vacuum. In combination with a pressure controlled throttle valve, these pumps are ideal for sputtering systems where high gas loads can damage the diffusion pumps, which is another pump used for this vacuum range. Its pumping rate is in the range of 50L/s to 2000L/s [34, 35].

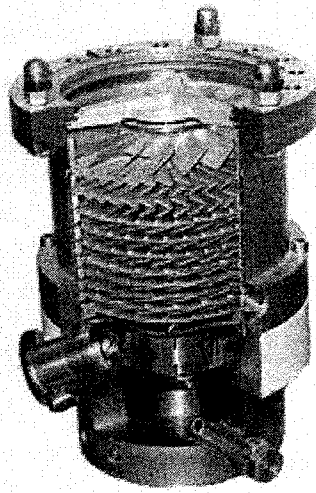


Figure 4. 2 A photograph showing the cross sectional view of a Turbomolecular pump [37].

4.1.2 Vacuum Chamber

A chamber is usually needed to keep the atmospheric gases and impurities away from the place where the deposition occurs. Usually a stainless steel or glass chamber is used because of its corrosion resistance, non magnetic characteristics and excellent outgassing characteristics. Stainless steel is preferred compared to a glass chamber because of its relatively high tensile strength, ease of welding and machinability [23, 33]. A stainless steel chamber (Figure 4.3) is used in our sputtering system.

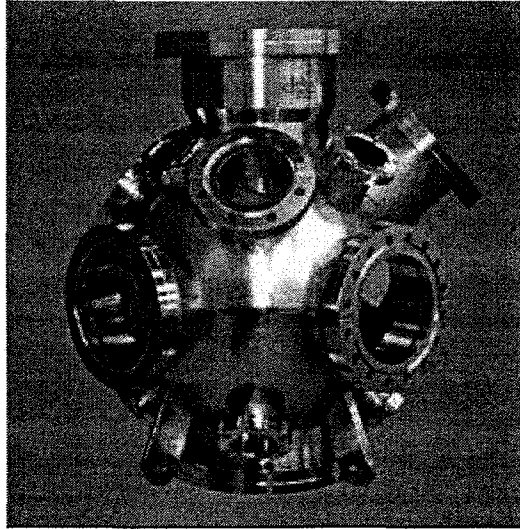


Figure 4. 3 A picture showing a typical vacuum chamber [39].

4.1.3 Pressure Gauges

The range of pressure measured in vacuum systems is very broad to be measured with a single vacuum gauge. In our sputtering system, two vacuum gauges, Convectron Gauge and Ionization gauge are used. A brief description of these groups is presented below.

4.1.3.1 Convectron Gauge

For this gauge, the measurement ranges from 10^{-3} torr to 1000 torr. It has a single gauge tube and a controller. The gauge tube contains a temperature compensated heat loss sensor which utilizes conduction cooling to sense pressure at lower pressures. At higher pressures, it utilizes convection cooling in which gas molecules are circulated through the gauge tube by gravitational force. It is individually calibrated and is known for its accurate and fast measurements. Convectron Gauges (Figure 4.4) are very reliable and they are recalibrated for contaminated gauge or after cleaning gauge. They are very stable [34, 35].



Figure 4. 4 A photograph of a Digital Convectron Gauge Controller [48].

4.1.3.2 Ionization Gauge

The main method for measuring pressure from 10^{-4} torr to 10^{-12} torr is gas ionization and ion collection/measurement. These gauges are divided in to two types: Cold Cathode and Hot Cathode. A heated filament emits electrons, which strike the gas molecules and ionize them. The positive ions are collected at a cathode, and the current produced is linearly related to the gas pressure. The ionization gauge (Figure 4.5) is not activated until the system pressure is below 5×10^{-4} torr. Ionization of gas by a high voltage results in a current of charges particles [34, 35].

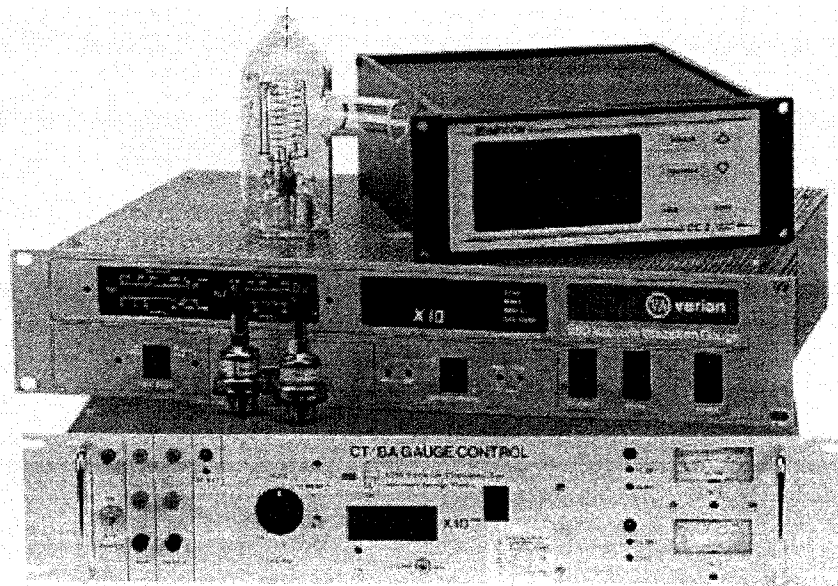


Figure 4. 5 A photograph showing an Ionization Gauge [49].

4.1.4 Target

Target is the material that is to be sputter deposited on to the substrate. The size and shape of the target depends on the material to be deposited, mode of sputtering, and the sputtering system design. Commonly used target shapes (Figure 4.6) are rectangular plates, discs, rings and tubes and their sizes vary from several inches to several feet long. The target material can be anything depending on the requirement. In our case we had hemispherical boron 10 as the target due to availability of this expensive material in this shape [24].

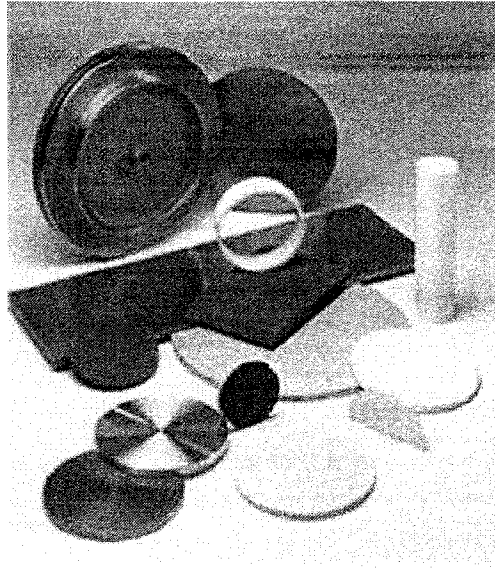


Figure 4. 6 A photograph showing conventional targets [52].

4.1.5 Sputter Head

Sputter head houses the target in a sputtering system. The sputter heads (Figure 4.7) are designed in a variety of configurations. The four essential design considerations for sputter heads are (1) heat dissipation, (2) electrical contact and isolation, (3) material of construction and (4) dark space shield/electron capture shield [33].

Around 75% of the energy incident on the target surface goes in to heating the target, 1% in to the ejection of sputtered atoms and the remaining is dissipated by secondary electrons that bombard and heat the substrate by the heat of condensation, recombination, recondensation and by plasma heating. Hence the targets should be water cooled [33]. Isolation of target assembly from grounded parts of sputtering system usually involves an insulating feed through. Water lines must be isolated from ground by using insulating tubing in series with water lines. Electrical connectors and switching mechanisms (RF and DC) must be designed for minimal power losses [33].

Many materials are used in constructing sputter head. The most common are stainless steel and copper. Stainless steel is corrosion resistant but has poor thermal conductivity. Whereas copper has excellent heat conductivity but corrosion is a problem [33]. To prevent sputtering on structural parts of the cathode assembly, a shield is placed around all such surfaces to protect them. The shield is placed from the cathode at a distance less than that of the Crooks dark space, hence, these shields are called “dark space shields”. No discharge will take place between two surfaces that have a space less than the Crooks dark space [33]. Experience with sputtering shows that the outer rim of the target face is subjected to greater erosion than the rest of the target because of the annular shape of the plasma. The glow discharge region of maximum intensity is an annular ring above the target surface. Therefore sputtering from target also occurs from the ring shaped region of the target immediately beneath the intense plasma ring.

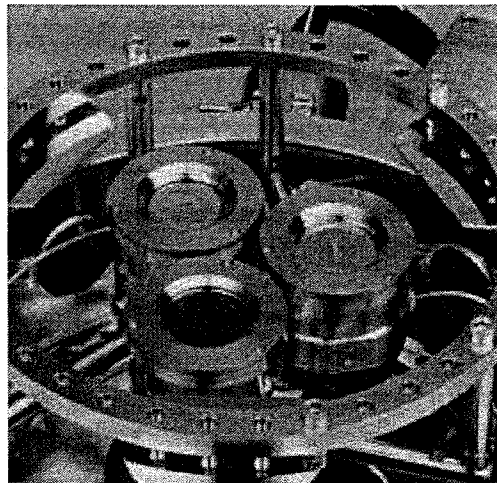


Figure 4. 7 A picture showing conventional three sputter heads [47].

4.1.6 Power Supply

Power supply for sputtering system can be either DC or RF. The selection of power supply depends on the type of sputtering to be performed and the material to be deposited. The main purpose of the power supply is to generate plasma and to induce sputtering by setting up a negative charge on the surface of the target. Power supplies must have good stability and control. A DC power supply was used in our system. DC power supplies are designed to provide the rated current under short circuit conditions. Average power densities of DC magnetron supply (Figure 4.8) are usually very high. Usually the input voltage for such power supplies are 115VAC $\pm 10\%$ 50/60Hz and the input current is 12A at 1kW power (full power). The output voltage ranges from 0-1000V. The power supply allows three modes of regulation: power, voltage and current. It also allows us to set the output power, voltage, current and the ramp time [24, 38].

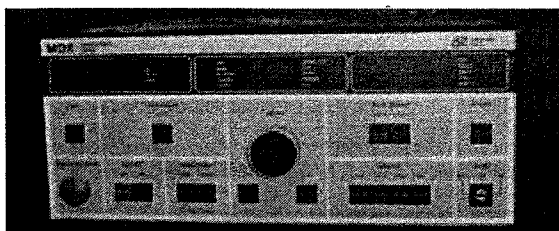


Figure 4. 8 A photograph of a DC Magnetron Power Supply [48].

4.2 Instruments used for Thin Film characterization and leak detection

In this section, a brief description of the film characterization and leak detection tools used is presented. The tools discussed are: (1) X Ray Fluorescence spectroscopy (2) Scanning Electron Microscopy and (3) Quadrupole Gas Analyzer/Residual Gas Analyzer.

4.2.1 X-ray Photoelectron Spectroscopy (XPS)

X-ray Photoelectron Spectroscopy (XPS) is also known as electron spectroscopy for chemical analysis (ESCA). It is a semi-quantitative technique for determining composition based on the photoelectric effect. XPS involves irradiation of the sample under vacuum by X-rays of known energy which causes photo-ejection of electrons from atoms near the surface. XPS uses a soft X-ray source ($AlK\alpha$ and $MgK\alpha$) to ionize electrons from the surface of a solid sample [40]. The binding energy of these electrons are measured and are characteristic of the elements and associated chemical bonds (chemical state) in the top few atomic layers of the material. The kinetic energy distribution of the emitted photoelectrons (i.e. the number of emitted photoelectrons as a function of their kinetic energy) can be measured using any appropriate electron energy analyzer and a photoelectron spectrum can thus be recorded [40]. For each and every element, there will be a characteristic binding energy associated with each core atomic orbital i.e. each element will give rise to a characteristic set of peaks in the photoelectron spectrum at kinetic energies determined by the photon energy and the respective binding energies. The presence of peaks at particular energies therefore indicates the presence of a specific element in the sample under study - furthermore, the intensity of the peaks is related to the concentration of the element within the sampled region. Atoms of a higher positive oxidation state exhibit a higher binding energy due to the extra columbic interaction between the photo-emitted electron and the ion core. This ability to discriminate between different oxidation states and chemical environments is one of the major strengths of the XPS technique.

An example XPS spectrum from Pd metal sample using Mg K_{α} radiation is shown in Figure 4.9. It is noted that from the area under the peaks corresponding to the element and comparing it to the XPS spectrum from elemental standards, one can obtain the elemental composition of the sample irradiated. A picture of an XPS setup is shown in Figure 4.10. XPS is used in this work for obtaining the composition of the sputtered films.

XPS facility available in the Desert research center was used for this research. The XPS instrument is a Surface Science Instruments SSX-100 with a Nonsequitur Technologies Model 1401 ion gun for sputtering. The XPS binding energies were referenced to the adventitious carbon $1s$ line at 284.6eV. The source for the XPS was a monochromatized aluminum K_{α} (1486 eV) source with a 0.5-1.0mm diameter X-ray spot size.

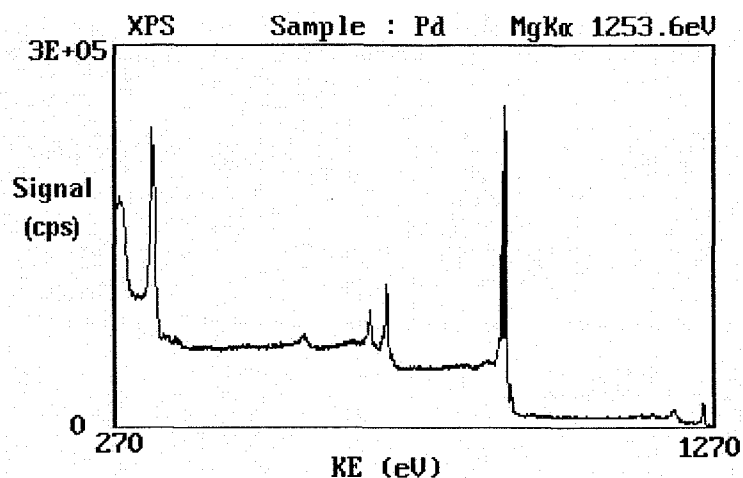


Figure 4. 9 An XPS spectrum obtained from a Pd metal sample using Mg K_{α} radiation

[40].

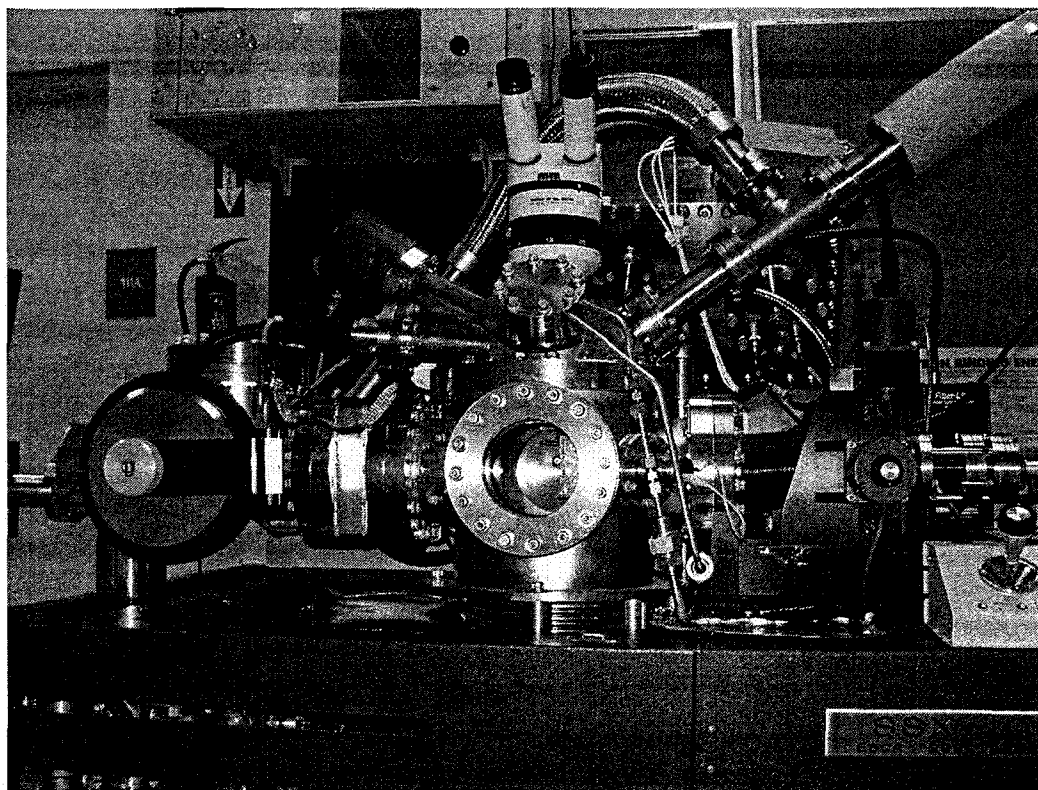


Figure 4. 10 A photograph showing our XPS setup.

4.2.2 Scanning Electron Microscopy (SEM)

I SEM as Microscope

In a typical SEM (Figure 4.11), electrons are thermionically emitted from tungsten or lanthanum hexaboride (LaB_6) cathode and are accelerated towards an anode using a high voltage (10kV to 100kV). Alternatively, electrons can be emitted via field emission (FE). Tungsten is used because of its highest melting point and lowest vapor pressure of all metals, thereby allowing it to be heated for electron emission. The electron beam, which typically has an energy ranging from a few hundred eV to 50keV, is focused by one or two condenser lenses into a beam with a very fine focal spot sized 1nm to 5nm. The beam passes through pairs of scanning coils in the objective lens, which deflect the beam in a

raster fashion over a rectangular area of the sample surface. Through scattering events by the constituent atoms of the material, the primary electron beam effectively spreads to a teardrop-shaped volume, called as the interaction volume [46]. The interaction volume can range from less than 100nm to 5 μ m into the surface depending on the energy of the incident beam and the atomic number of the constituents of the material. This type of interactions results in emission of backscattered and secondary electrons which are then, detected to produce a spatial image [43].

II SEM as Energy-dispersive X-ray spectroscopy

Interaction of primary electrons with the constituent atoms also produces X-rays which are specific characteristics of the constituents. This can be used for compositional analysis. At rest, an atom within the sample contains ground state ('unexcited') electrons situated in concentric shells around the nucleus. The incident beam, however, excites an electron in an inner shell, prompting its ejection and resulting in the formation of an electron hole within the atom's electronic structure. An electron from an outer, higher-energy shell then fills the hole, and the excess energy of that electron is released in the form of an X-ray. The release of X-rays creates spectral lines that are highly specific to individual elements. Thus, the X-ray emission data can be analyzed to characterize the sample [43].

III SEM for Thin Film Thickness Measurement

The cross section of the sample to be measured is placed using a special type of sample holder in a SEM. The signals which make up SEM image are generated via the interaction of illumination (a focused beam of high-energy electrons) with the atomic structure of the sample (the actual protons, neutrons, and electrons that make up all

matter). These imaging signals come in two basic forms. They are: (1) SECONDARY ELECTRONS (SE), which are created by collisions between the high-energy electrons in the illuminating beam (so-called "primary" electrons) and the electrons which surround the atoms in the sample. Such collisions knock the low-energy electrons out of their orbits, (2) BACKSCATTERED ELECTRONS (BSE), which are created by collisions between the primary beam electrons and the nuclei of the target atoms. These collisions result in the primary electrons bouncing off of the larger, more massive nuclei [51]. The obtained image after scanning shows a color contrast between the thin film and the substrate depending on the average atomic number of the constituent atoms. The contrast between the film and the substrate can be used to measure the thickness of the film.

IV Sample Preparation

One of the great strength of SEM is the fact that many specimens can be examined with virtually no specimen preparation. Conductive Coating is necessary to eliminate or reduce the electric charge that builds up rapidly in a nonconductive specimen when it is scanned by a beam of high-energy electrons. The charging phenomena results in image distortion, the primary beam can also cause thermal and radiation damage depending on the beam energy and the material it interacts with, which can lead to a significant loss of material from the specimen. For medium-resolution SEM (spatial resolutions 3-5nm), either gold-palladium or platinum-iridium coating on insulating material specimens gives the best result [44].

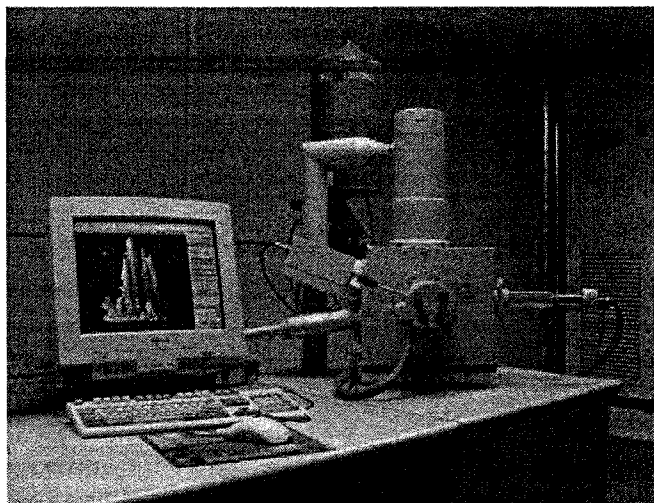


Figure 4. 11 A photograph showing a typical SEM [45].

SEM was used in this work to find the thickness and chemical composition of the sputtered films. The SEM at EMIL, UNLV is JEOL JSM-5610 with an Oxford EDS detector. It has resolution of 3.5nm and specimen size less than 150nm. The detectable element range is from ${}^5\text{B}$ to ${}^{92}\text{U}$. It has a W filament electron gun and accelerating voltage up to 30kV. The oxford ISIS EDS system is capable of qualitative, pseudo-quantitative analyses, and x-ray mapping.

4.2.3 Quadrupole Gas Analyzer/Residual Gas Analyzer

A residual gas analyzer is a small and a rugged mass spectrometer that measures the individual partial pressures of gases in a mixture. RGAs determine the gases present in the vacuum environments by separating, identifying and measuring the quantity of all gas molecules in the vacuum system. The RGA system includes a sensor, which operates under high vacuum, the electronics, which operate the sensor, and software, working in conjunction with an external computer to display data and control the electronics [50]. The RGA sensor consists of three parts:

Ion source: The ion source contains a heated filament that emits electrons. These electrons collide with gas molecules in the vacuum system, giving them an electrical charge, which produces ions.

Quadrupole Mass Filter: Ions produced in the ion source move into the quadrupole mass filter to be separated according to their mass-to-charge ratio.

Ion Detector: Ions that have been transmitted through the quadrupole mass filter strike the detector, become neutralized, and draw a current that is proportional to and identifies the gas component present.

RGAs are used in most cases to monitor the quality of the vacuum and easily detect minute traces of impurities in the low pressure gas environment. These impurities can be measured down to 10^{-14} torr levels [24]. Utilizing quadrupole technology, there exists two implementations utilizing either an open ion source (OIS) or a closed ion source (CIS). RGAs (Figure 4.12) are also used in evaporators, sputterers, etchers or any other high vacuum systems that are routinely pumped down to lower than 10^{-5} torr. Their main application is to check the integrity of the vacuum seals and the quality of the vacuum before any deposition process. Air leaks, virtual leaks and many other contaminants at very low levels can ruin the quality of deposition and must be detected before a process is initiated [41]. RGA was used in this work to chemically characterize the residual gas in the growth chamber before sputtering.

The RGA used in this work is a LC series Residual gas analyzer. It has a mass range of 1 – 100AMU and operating pressure range of 10^{-4} torr. The emission current ranges from 0.1 to 10mA and ion energy of 1 to 10V. The minimum partial pressure it can detect is 5×10^{-12} torr.

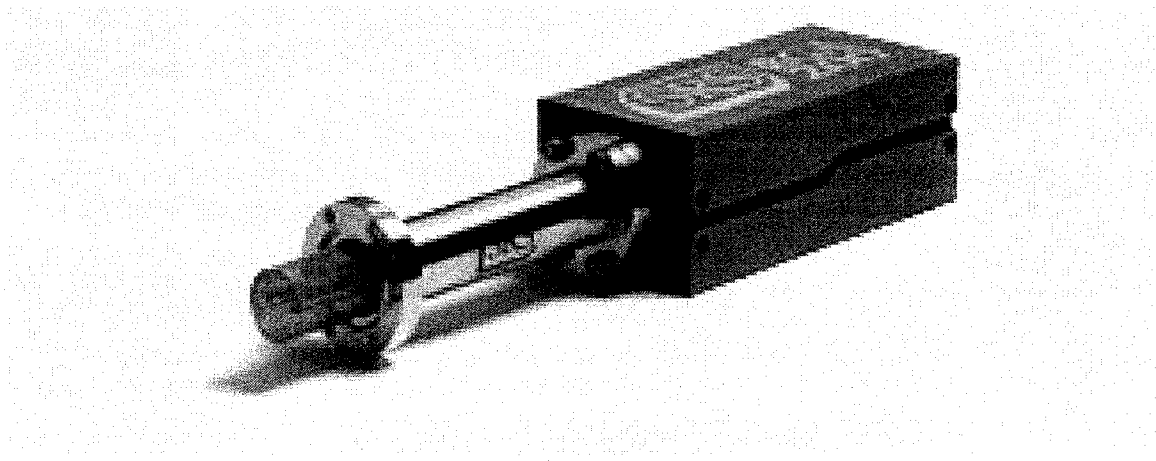


Figure 4. 12 A photograph showing a typical RGA [42].

CHAPTER 5

DESIGN OF SPUTTERING SYSTEM

Design of sputtering system was accomplished in two steps, paper design and actual design using steel, Boron 10 (^{10}B) target components. Details of these two steps are presented in this section. Also, the experimental procedure for the sputtering process is presented.

5.1 Paper Design

Paper design was done to develop the mechanical drawings of all the subcomponents of the sputter head. The CAD software used for this purpose is SOLIDWORKS. The other component of the paper design was to investigate the electrostatic and magnetostatic fields of the sputtering system in order to make sure the field conditions within the sputtering system was sufficient to ignite an Ar plasma based on the Pashen curve (break down voltage versus the pressure-distance plot) for Ar plasma.

5.1.1 SOLIDWORKS 2006

SolidWorks is a computer aided design program with particular emphasis on 3 dimensional mechanical designs of components. It runs on the Microsoft Windows platforms. It provides design solutions, analysis tools to simulate real-world conditions and allow different scenarios to be tested. It also facilitates design communication and collaboration, and use of private and public libraries in design solutions.

Since our target material is a hemispherical shell of ^{10}B (Figure 5.3), a special magnetron head with a cylindrical Nd-Fe-B permanent magnet was designed. The head consists of a hollow cylinder with bottom made of SS-410 (Figure 5.1). The inner diameter, outer diameter and the bottom thickness are 56mm, 72mm and 27mm, respectively. Four through holes of diameter 5mm were drilled symmetrically at a distance of 18.50mm from the center of the bottom. These holes are used to attach the cylinder to a copper plate (Figure 5.2), which is connected to the electrode through a copper rod of length 100mm. The hemispherical target was clamped to the SS-410 housing by drilling eight holes around the housing. Eight screws were then used to attach the target to the housing. A mechanical drawing showing the elevation, planar and side views of the cylinder is presented in Figure 5.1. An Nd-Fe-B cylindrical permanent magnet was used in our system to increase the ionizing collision of electrons by utilizing the magnetic fields to help them confine the electrons near the target surface. SS-410 which is ferromagnetic was used in the system to close the magnetic field lines from the permanent magnet.

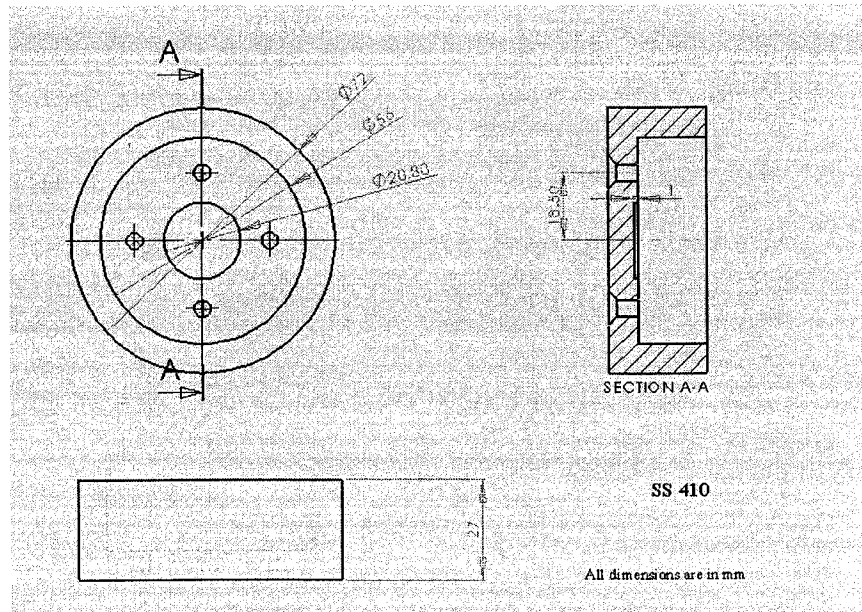


Figure 5. 1 Mechanical drawings of the SS-410 stainless steel cylinder.

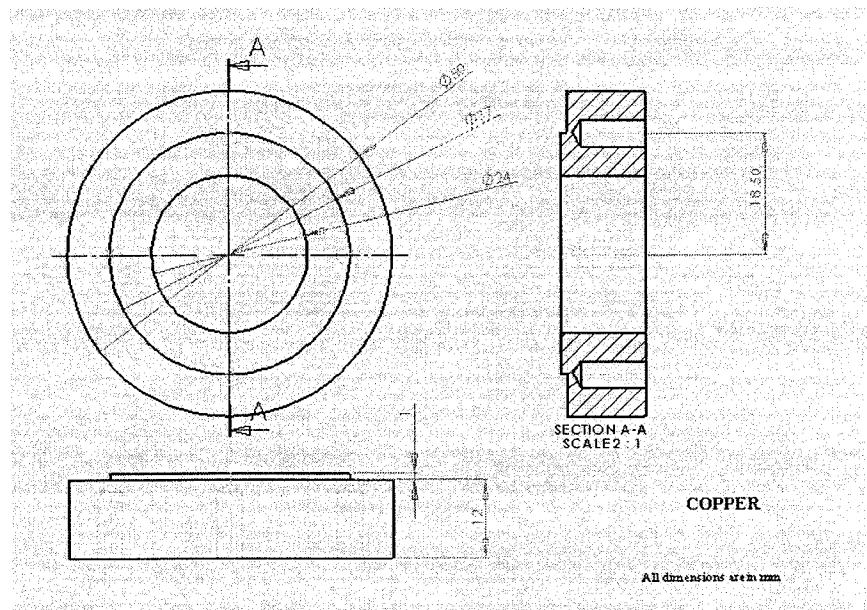


Figure 5. 2 Mechanical drawings of the copper ring.

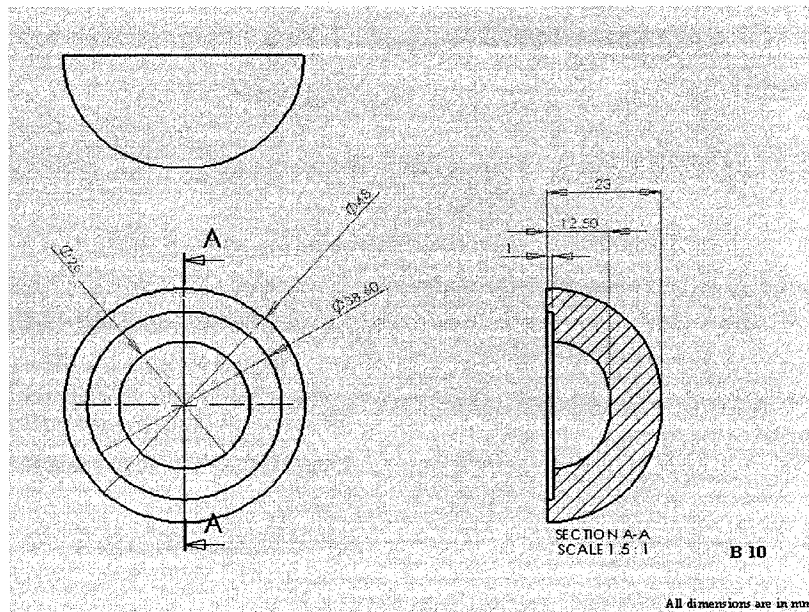


Figure 5.3 Mechanical drawings of the hemispherical Boron 10 dome.

Our system requires a permanent magnet (Nd-Fe-B) to be placed in the middle of the stainless steel cylinder, underneath the hemispherical dome which is 48mm in diameter (Figure 5.3). Since the magnet is very strong, it gets attached strongly to any ferro-magnetic materials in close proximity. Thus if the magnet is not placed exactly in the middle, it will get attached in the wrong position and it is very difficult to dislodge it. Thus, it is very important that the permanent magnet be placed carefully in the middle of the cylinder. To ensure this, an Aluminum sleeve of inner diameter equal to that of the outer diameter of the cylindrical permanent magnet which is 20.8mm and outer diameter equal to the inner diameter of the hollow cylinder was machined. Mechanical drawings of the aluminum sleeve is shown in Figure 5.4.

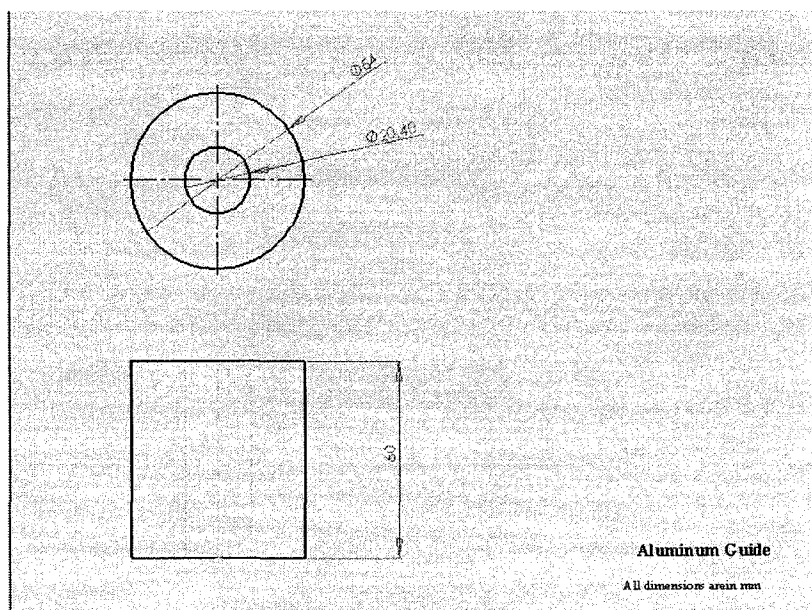


Figure 5. 4 A mechanical drawings of the aluminum sleeve used for sliding the permanent magnet in to its place in the SS-410 cylinder.

A mechanical drawing of the aluminum sleeve which is placed inside the hollow steel cylinder is shown in Figure 5.5. When the permanent magnet is dropped, it slides on the walls of the aluminum and places itself exactly in the middle of the cylinder where there is a concentric small recess of depth 1mm of the cylinder at the bottom. Figure 5.6 and Figure 5.7 shows a 3D view of the arrangement of the sputter head with the hemispherical ^{10}B target.

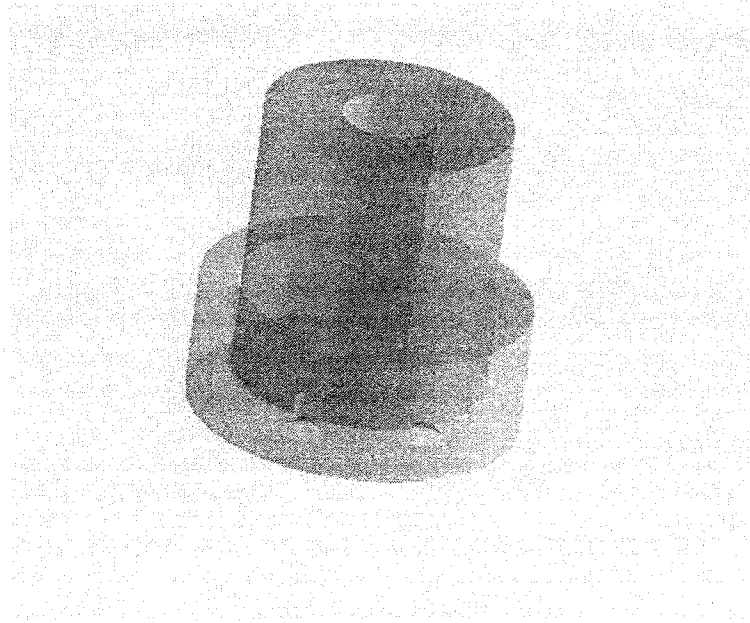


Figure 5. 5 A 3-D view of the Aluminum sleeve with SS-410.

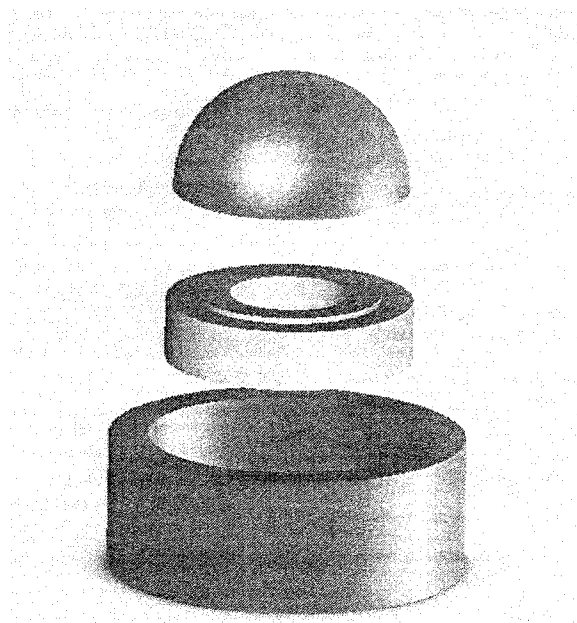


Figure 5. 6 A 3-D view showing the arrangement of the sputter head set-up.

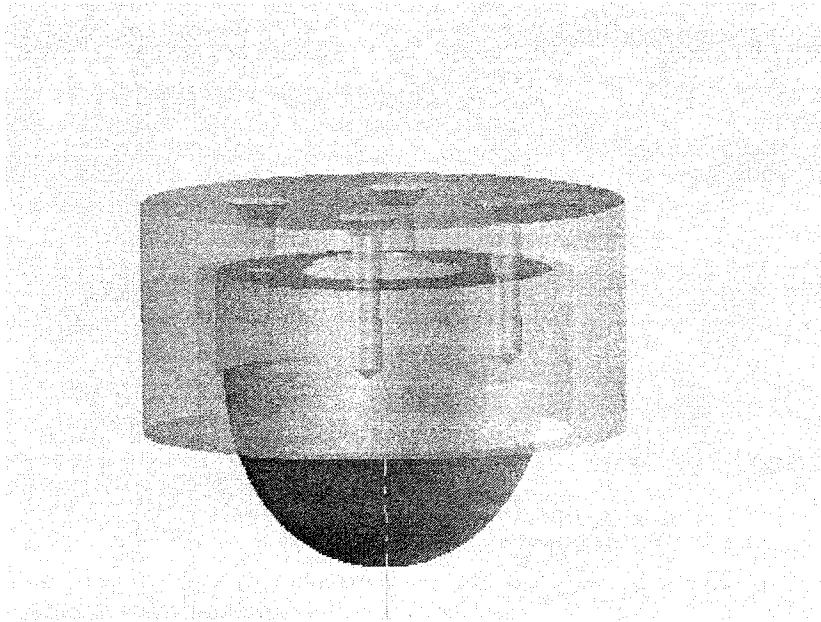


Figure 5. 7 A 3-D view of the sputter head set-up with the hemispherical target.

5.1.2 TRICOMP 6.0

TRICOMP 6.0 (2D) is computational software, which solves problems in electrostatics, magnetostatics, thermal transport, charged-particle gun design and transport and electromagnetic pulses in to 2D and 3D cylindrically. The electrostatic and magneto static analysis of the sputtering system was done using this software. Since the sputtering system is axially symmetric, only one half of the system was simulated. The software uses advanced finite-element methods to solve for the electrostatics.

The first step in the simulation is to create a mesh for the structure that needs to be simulated. For creating a mesh in TRICOMP 6.0, MESH 6.0 program was executed and the dimensions and the geometry of the structure from the mechanical design software were loaded in to it to get the final mesh structure. Figure 5.8 shows a picture of mesh generated for our structure.

The inner diameter, outer diameter and the bottom thickness of the SS-410 cylinder are, 56mm, 72mm and 27mm, respectively. The inner and outer diameter of the hemispherical ^{10}B target is, 25mm and 47mm, respectively. The height and diameter of the permanent magnet is, 25.9mm and 10mm, respectively. The distance between the ^{10}B target and the sample holder is roughly 35mm.

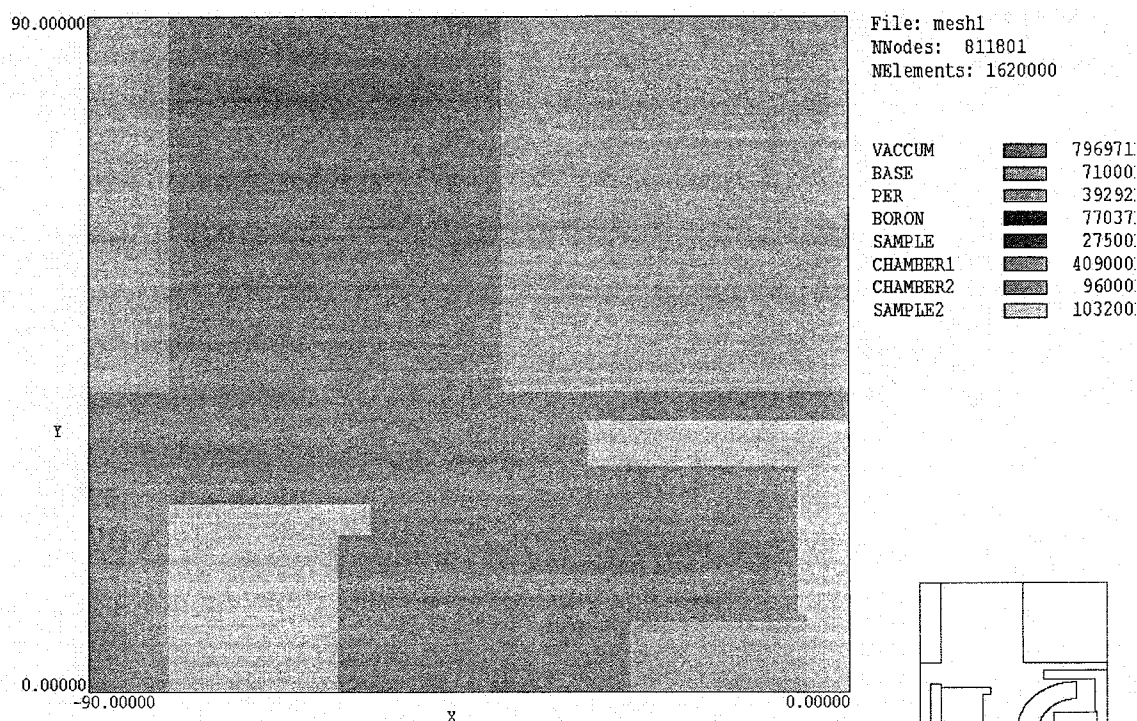


Figure 5. 8 A 2-D view of the mesh generated for the sputtering setup using MESH 6.0 program of TRICOMP 6.0.

The second step is to do an electrostatic analysis of the mesh generated from MESH 6.0. To accomplish this step, the output file from MESH 6.0 (which contains information about the mesh structure) was loaded to ESTAT 6.0 program. In this program, the electrical properties of the material such as conductivity and permittivity are used in the system were supplied. Cylindrical geometry is used for this simulation. Relative

permittivity of vacuum is taken to be 1. The electrostatic potential applied on the base, permanent magnet and ^{10}B is 290V and electrostatic potential on the sample holder and the substrate walls are 0V. A complete electrostatic analysis of the structure is done in this program. Figure 5.9 shows the pattern of the electrostatic field lines present in sputtering system. It can be seen from Figure 5.9 that the electrostatic potential is very intense near the hemispherical dome i.e. in the order of 37.0V and it gradually starts to decrease away from the dome. The electrostatic field lines seem to be zigzag between the dome and SS-410 but, it seems to be uniform outside the dome.

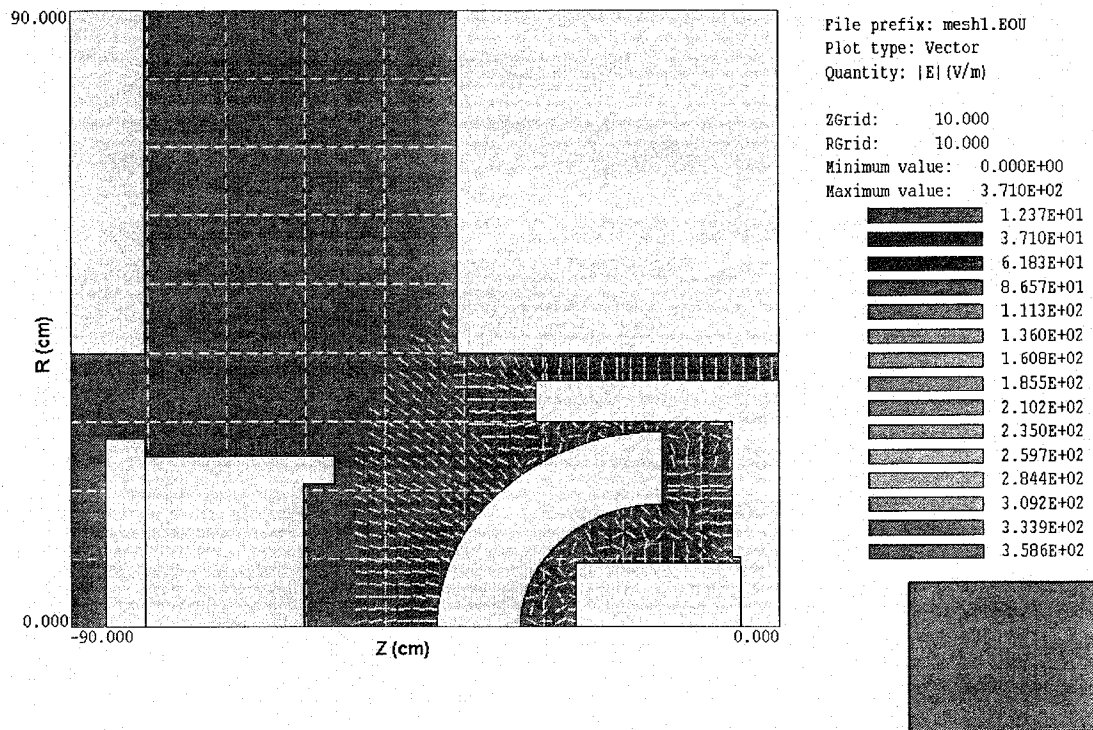


Figure 5. 9 A 2-D view of the electrostatic field lines generated using ESTAT 6.0 for the sputtering setup.

The third step is to perform a magnetostatic analysis of the mesh generated from MESH 6.0. To accomplish this, the output file from MESH 6.0 is loaded in to PerMag 6.0. program. Again in this program the properties of the materials used were supplied. The permeabilities of the vacuum, sample holder and chamber are taken to be 1 and the relative permeability of SS-410 cylinder is taken to be 4000. A detailed magnetostatic analysis of the structure was performed. Figure 5.10 shows the pattern of the magnetic field lines obtained from Per Mag 6.0 program. The magnetic fields seem to be uniform throughout but it is very high around the permanent magnet. The magnetic field lines originating from the permanent magnet closes on the SS-410 cylinder.

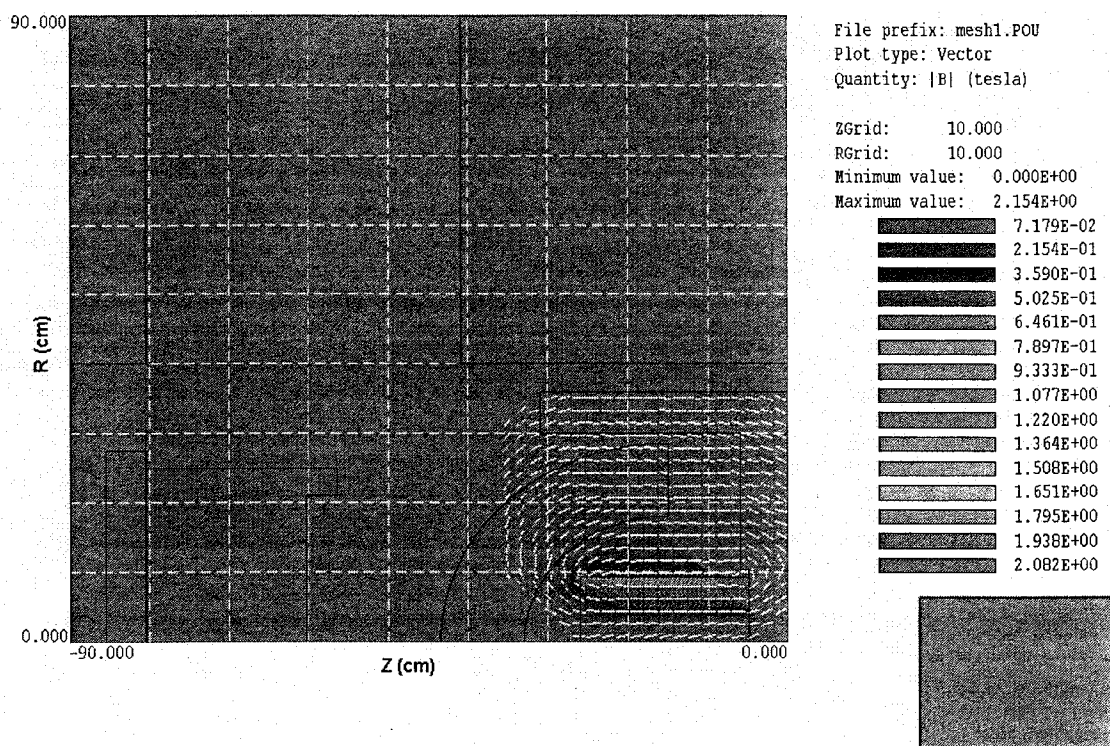


Figure 5. 10 A 2-D view of the magnetic field lines generated using PERMAG 6.0 for the sputtering setup.

Results of the electrostatic and the magnetostatic fields were analyzed and the dimensions of the various components were systematically changed to achieve the required electrostatic and magnetostatic fields. The dimensions of the components machined in section 5.1.1 were obtained by this procedure.

5.2 Manufacture of Components

The components used for the sputtering system were fabricated in the machine shop in the college of engineering. CNC (computer numerical control) machine in the machine shop was used to machine the SS-410 cylinder, copper ring, copper rods and to drill holes in the SS-410 cylinder to the dimensions obtained by the procedure and method described in section 5.1.2.

The sputter head consists of a hollow SS-410 cylinder with inner diameter of 56mm, outer diameter of 72mm and the bottom thickness of 27mm. Four through holes of diameter 5mm were drilled on the bottom of the cylinder symmetrically at a distance of 18.50mm from the center of the bottom. These holes are used to attach the cylinder to a 25mm by 25mm square copper plate which is connected to the electrode through a copper rod of length 100mm. Our system requires a permanent magnet (Nd-Fe-B) be placed in the middle of the stainless steel cylinder, underneath the hemispherical ^{10}B . An Aluminum sleeve (Figure 5.11) of inner diameter equal to that of the outer diameter of the magnet and outer diameter equal to the inner diameter of the hollow cylinder was machined. A glass ring of inner diameter 56mm and outer diameter 72mm was machined and attached to the top rim of the SS-410 cylinder. Two sets of experiments were carried

performed. One, without the glass ring and one, with the glass ring, which will be discussed in chapter 6.

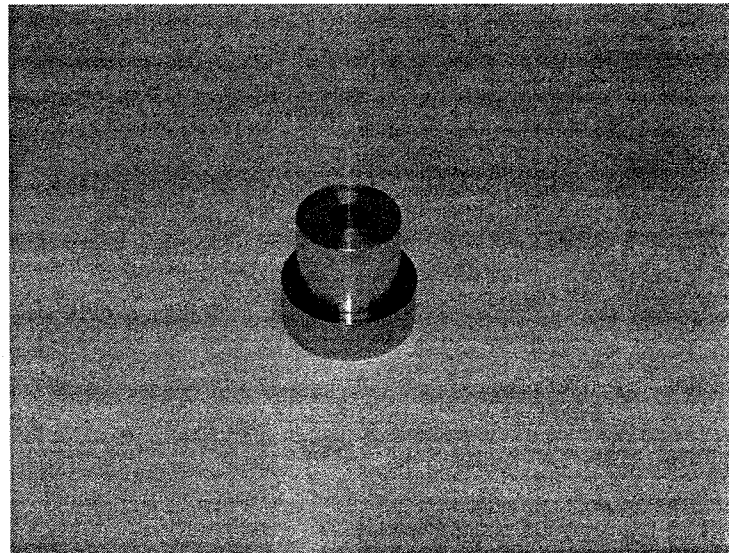


Figure 5. 11 A photograph showing how the Aluminum sleeve fits in SS-410 cylinder.

As discussed in section 5.1, if the magnet is not placed exactly in the middle, it will get attached in the wrong position on the SS-410 cylinder. Once it is attached to the wrong place, it is very difficult to dislodge it. Thus, it is very important that the permanent magnet be placed carefully in the middle of the cylinder. Figure 5.12 is a photograph depicting the placing of the permanent magnet inside the SS-410 cylinder. Figure 5.13 shows a picture of the placed permanent magnet on SS-410 cylinder.



Figure 5. 12 A photograph depicting the placing of the permanent magnet on SS-410.

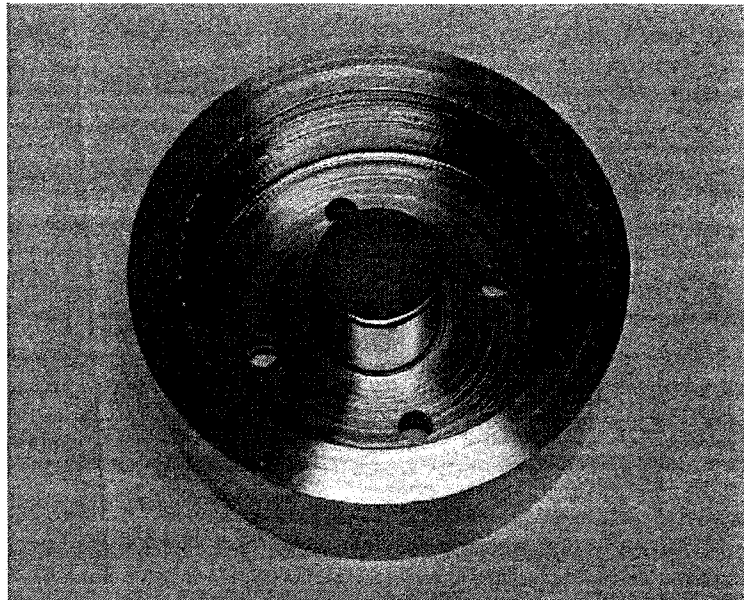


Figure 5. 13 A photograph of the permanent magnet placed exactly in the middle of the
SS-410 cylinder.

Initially the ^{10}B dome is placed on the copper ring (Figure 5.14) which, in turn, is placed on the SS-410 cylinder. Then, a copper ring is attached to the back of the SS-410 cylinder (Figure 5.15 and Figure 5.16). The complete sputter head set up is placed upside down, i.e., the ^{10}B dome is suspended upside down using the copper rod (Figure 5.17). Figures 5.18 and 5.19 are photographs of the outside view of the sputter chamber. At the top of the chamber, the cathode connection is seen. The turbo pump is on the right hand side of the vacuum gauge and RGA connection is seen on the left hand side. A complete view of the sputtering system with its mechanical support is shown in Figure 19. The mechanical pump is seen at the bottom. A block diagram of the whole sputtering system is shown in Figure 5.20.

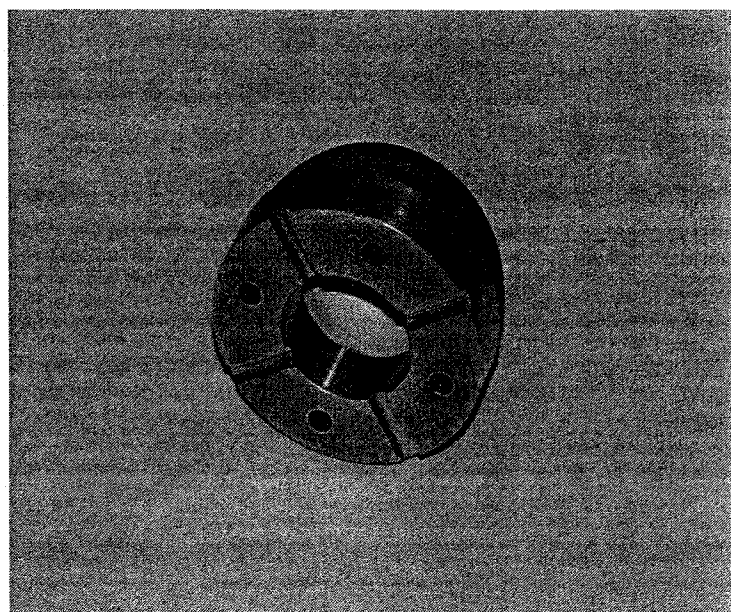


Figure 5. 14 A photograph of the copper ring with the ^{10}B dome on the top of it.

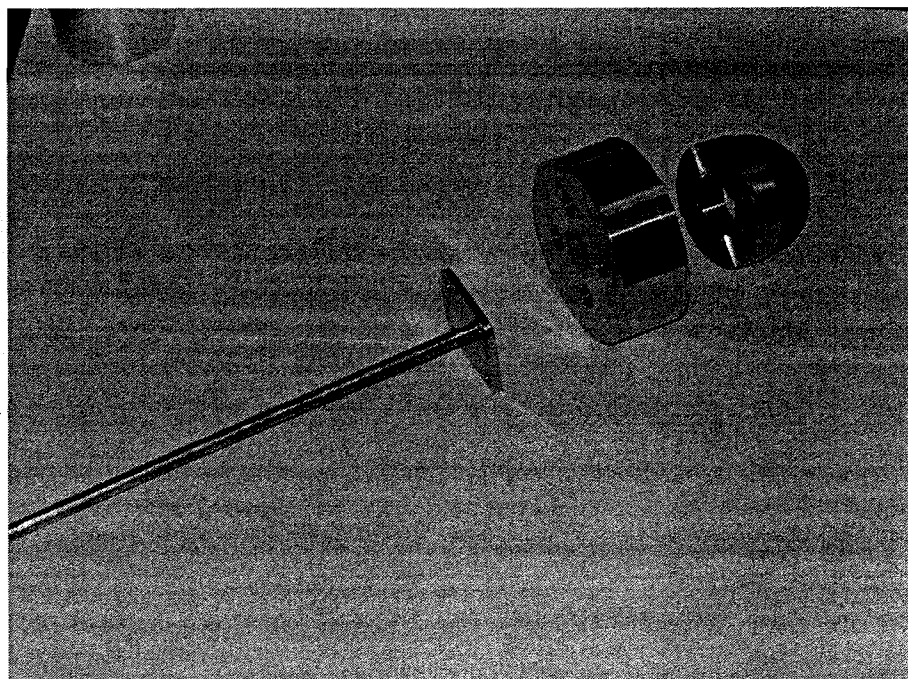


Figure 5. 15 A photograph showing the sputter head set-up with copper rod, SS-410, copper ring and the hemispherical boron 10 dome.

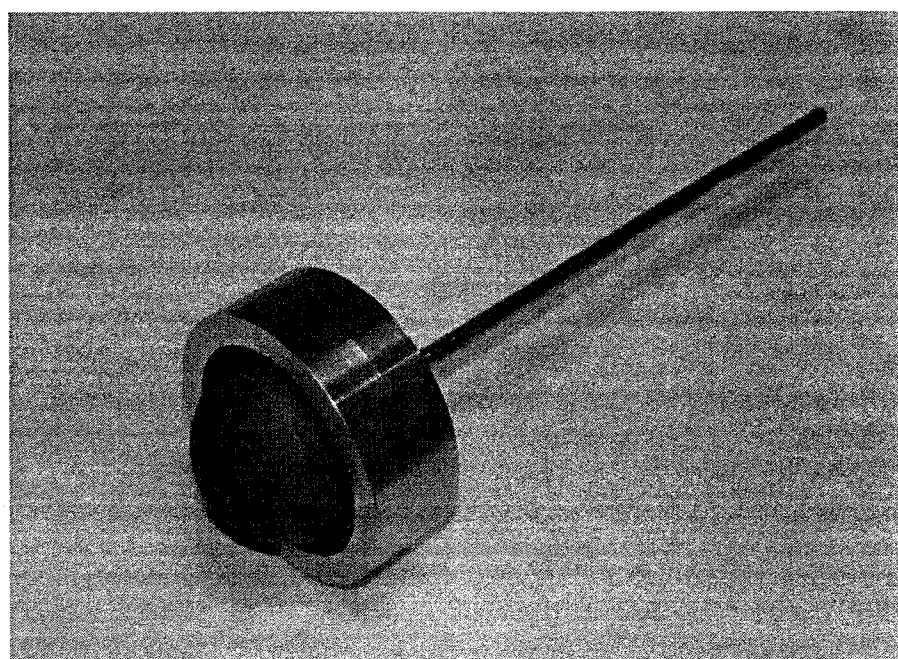


Figure 5. 16 A picture showing target set up with the copper rod.

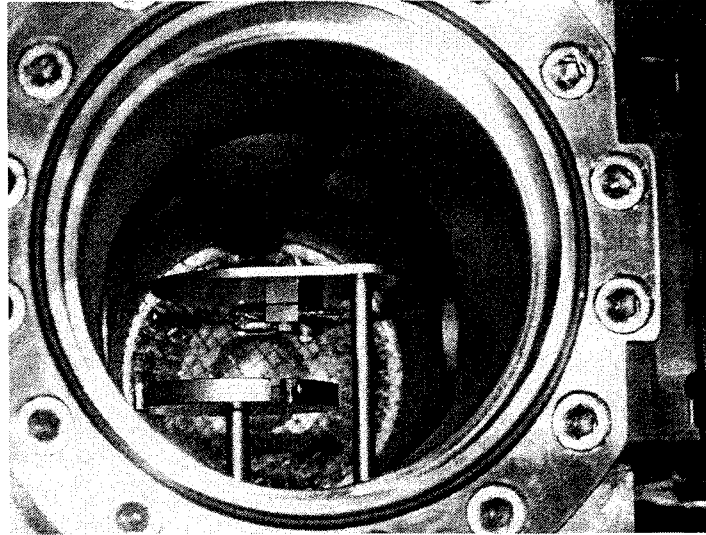


Figure 5. 17 A photograph of the side view of the sputter chamber showing the vertically suspended sputter head.

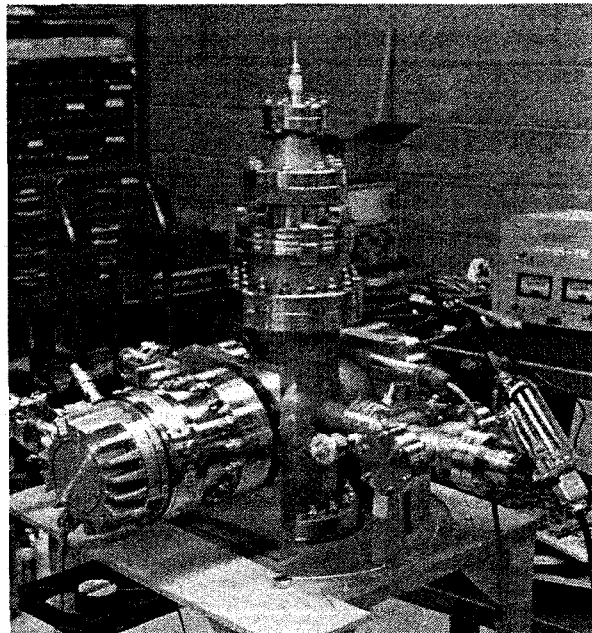


Figure 5. 18 A photographic view of the top portion of the sputter chamber with the turbo pump and high vacuum gauge.

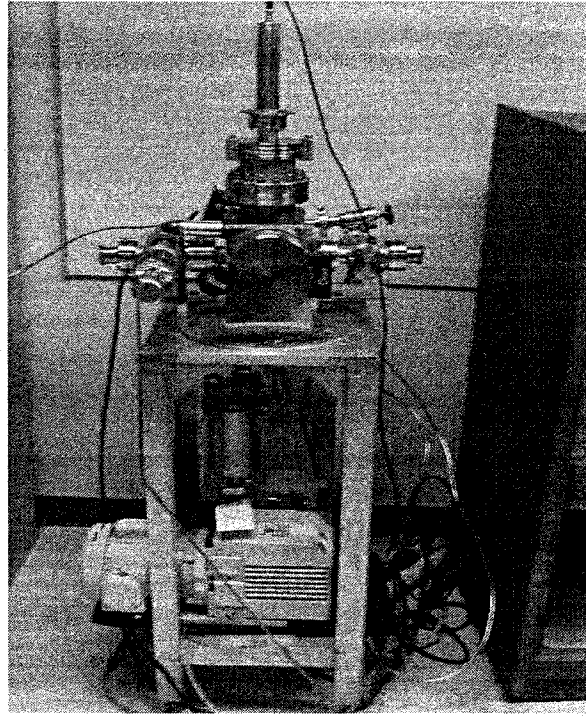


Figure 5. 19 A photographic view of the complete sputtering system showing the mechanical pump.

5.3 Experimental Procedure

A step by step procedure of operation of the sputtering system along with the safety issues are presented in Appendix A.

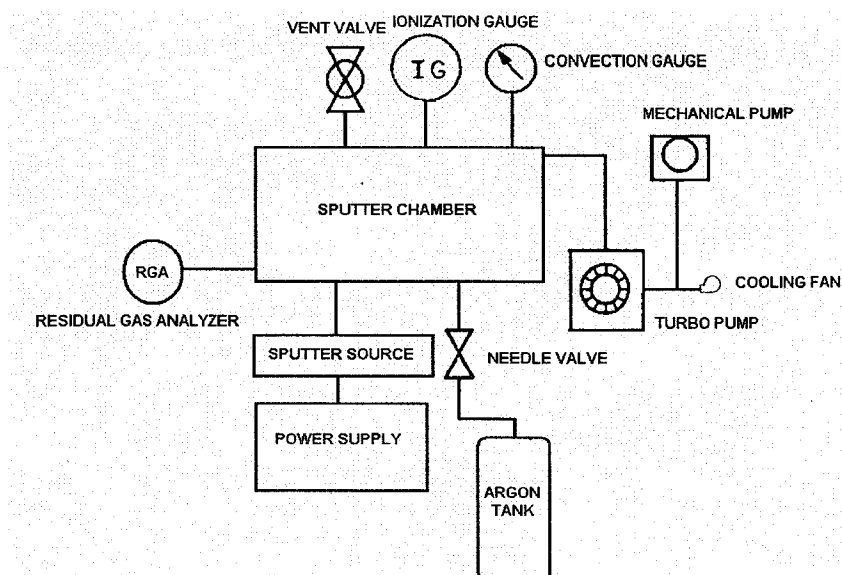


Figure 5. 20 A schematic block diagram of the whole sputtering system.

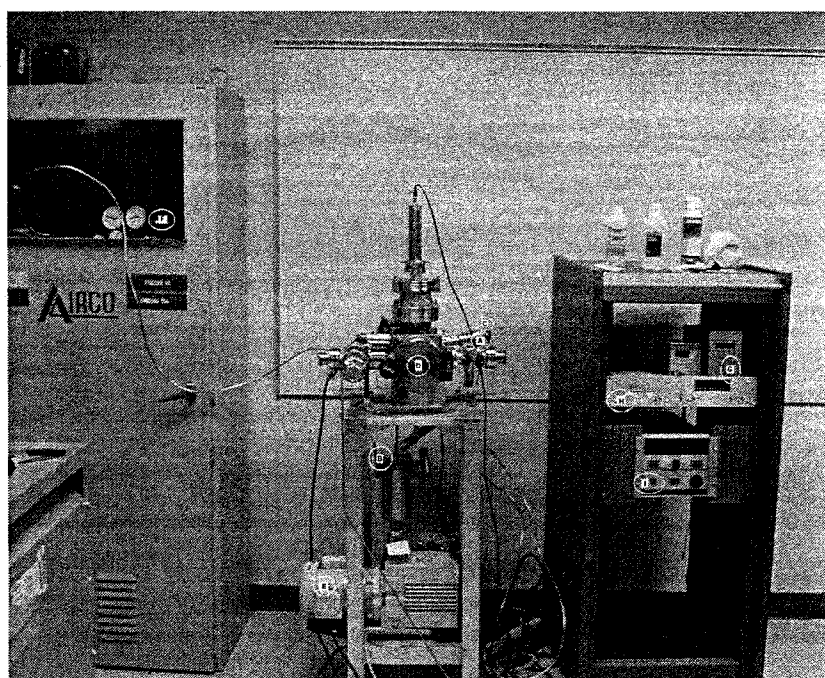


Figure 5. 21 A photographic view of the complete sputtering system with the power supply.

CHAPTER 6

RESULTS AND DISCUSSIONS

Boron 10 (^{10}B) thin films were deposited on glass and silicon substrates using RF magnetron sputtering on silicon substrate. Deposition was carried out at two different conditions, one with Ar partial pressure of $P_{\text{Ar}} = 25\text{mtorr}$, current, $I = 0.009\text{A}$, voltage, $V = 290\text{V}$ and the other with $P_{\text{Ar}} = 10\text{mtorr}$, current, $I = 0.009\text{A}$, voltage, $V = 290\text{V}$. The composition and the thickness of these films were analyzed using Scanning electron microscope and XPS. Vacuum leak check was performed using a quadrupole mass analyzer.

6.1 Results

I Scanning electron microscope

The cross-sectional sample was placed in the sample holder with the orientation showing the deposited ^{10}B film, its thickness and the interface between the film and the substrate. The photograph shown in Figure 6.1 and 6.2 shows the cross section of the thin film deposited at 25mtorr and 10mtorr, respectively. The micrographs were taken at 25,000X and 11,000X, for Figures 6.1 and 6.2 respectively. Thickness of the film measured by SEM shown in Figures 6.1 and 6.2 are $1.0\mu\text{m}$ and $0.9\mu\text{m}$, respectively.

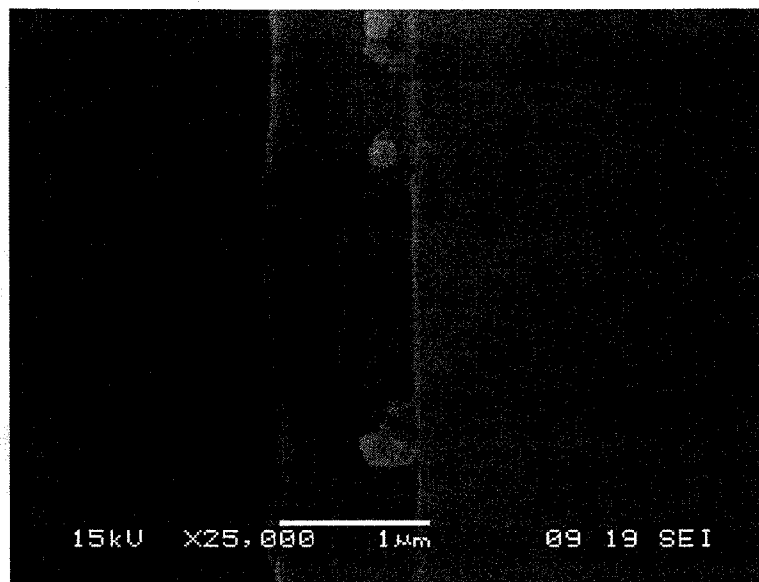


Figure 6. 1 A photograph of an SEM image showing the thickness of the deposited ^{10}B film at a magnification of 25,000X.

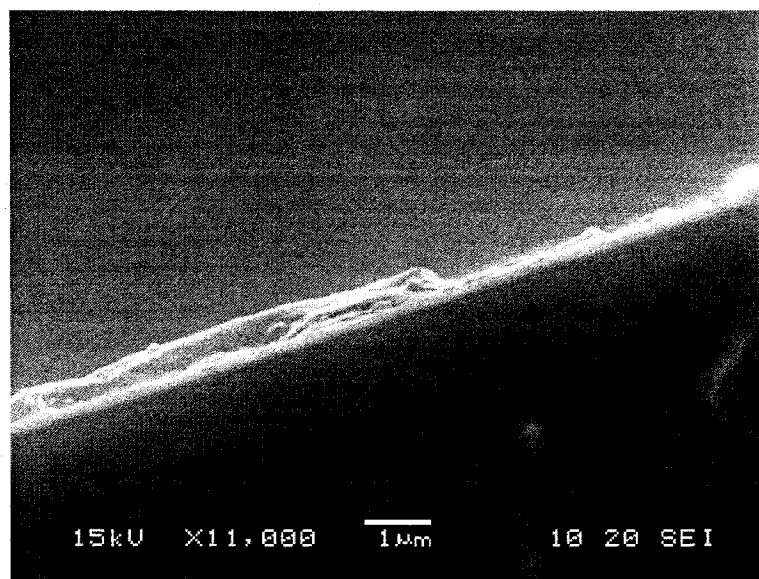


Figure 6. 2 A photograph of an SEM image showing the thickness of the deposited ^{10}B film at a magnification of 11,000X.

The Oxford EDS detector investigations (Figure 6.3 and 6.4) revealed that there is silicon peak in the spectrum. This is consistent as the substrate is silicon and the volume of interaction of the electron beam definitely extends in to the silicon substrate. The spectrum also shows a Copper and oxygen peak. The copper is mainly from the copper ring in the sputter head or from the brass of the SEM sample holder. The oxygen may be due to a possible vacuum leak or from the water vapor left in the sputter chamber. A vacuum leak check was performed using a quadrupole gas analyzer and the results are discussed in section IV. Gold is observed in the spectrum, which is due to the gold coating on the sample used for preventing charging of the sample by the electron beam. In Figure 6.4, a small ^{10}B peak was observed. Typically, it is very difficult to observe boron related peaks in SEM-EDS due to the low atomic number of boron. XPS analysis was done to identify all the elements in the film, knowing that boron is at the lower end of atomic numbers that can be detected. We always observe a peak at 0 keV. The peak is the check signal. It doesn't have any meaning and it is always at the same height in all the scans.

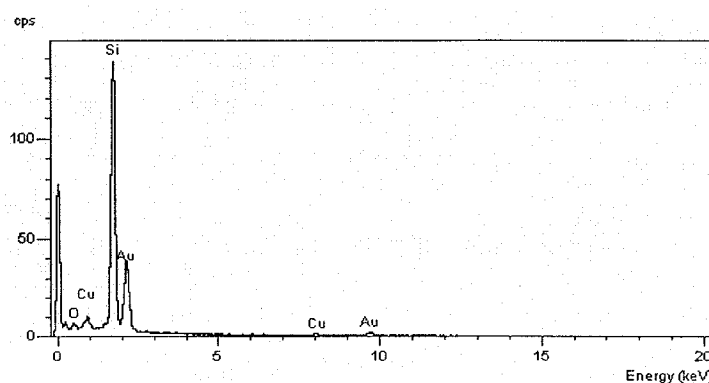


Figure 6. 3 EDS high-resolution plot of energy (keV) versus counts per second obtained from sputtered film.

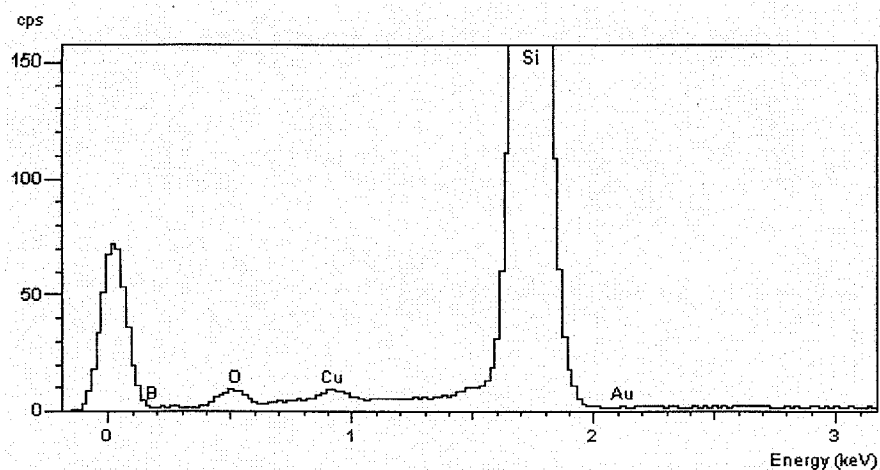


Figure 6. 4 EDS high-resolution plot of energy (keV) versus counts per second obtained from sputtered film.

III X-RAY Photoelectron spectroscopy

The XPS spectrum (Figure 6.5 and 6.7) is a plot of binding energy versus counts. The spectrum shown in Figure 6.5 indicates that there is a large percentage (around 50%) of iron in the sample. The deposited film has around 19.69% ^{10}B , 10.81% oxygen and 11.61% carbon. These films were deposited at a pressure of 10mtorr. In order to eliminate the presence of iron, we attached a glass ring to the SS-410 cylinder using epoxy glue (Figure 6.6). The glass ring acts like a mask for SS-410, thereby avoiding the sputtering of Iron. Glass was chosen because, glass is an insulator and the accumulated charges on the glass ring will repel the argon ions away from it. Therefore, the argon ions will be more confined to the target surface. The spectrum in Figure 6.7 shows 65% oxygen, 19.46% of boron, 1.31% carbon and no iron were found in the sample. The conditions of deposition changed from a pressure of 10mtorr to 25mtorr when the glass ring was attached. Figure 6.8 is the XPS spectra of the ^{10}B hemispherical target itself. It

can be seen that the target itself contains only 18.96% boron but it contains 47.01% carbon. This is one of the main reasons for the presence of carbon in the deposited thin film. It is interesting to note that the target contains less oxygen, but the deposited film contains a large percentage of oxygen. The origin of oxygen should be from a vacuum leak or water vapor in the chamber. This issue will be discussed and resolved in section IV. The error bars of these scans are one to two tenths of an electron volt for energy and 5% for count rate. Our XPS sample was sputter cleaned for 5 to 10 seconds with argon gas at an energy of 5keV and a current density of 10mA at our XPS set up to eliminate the contamination from the atmosphere while transporting the sample from our lab to the XPS lab. Furthermore, different elements have different sputter yields. Therefore, the compositions of the deposited films vary as a function of sputter time and current density. Since we sputter cleaned only for a few seconds the composition of the film is assumed to not have been affected.

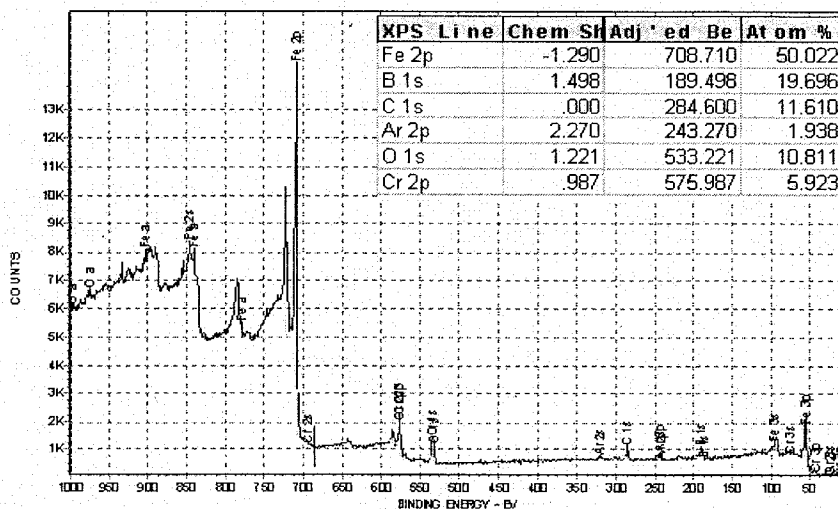


Figure 6. 5 XPS spectra of binding energy versus counts for a typical sample without the glass ring.

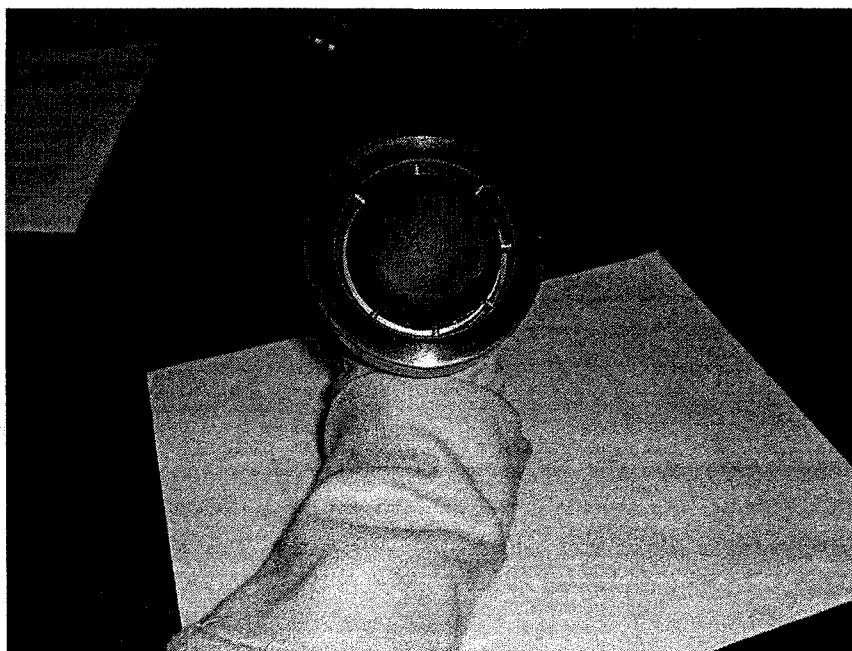


Figure 6. 6 A photograph showing the sputter head set-up with the glass ring

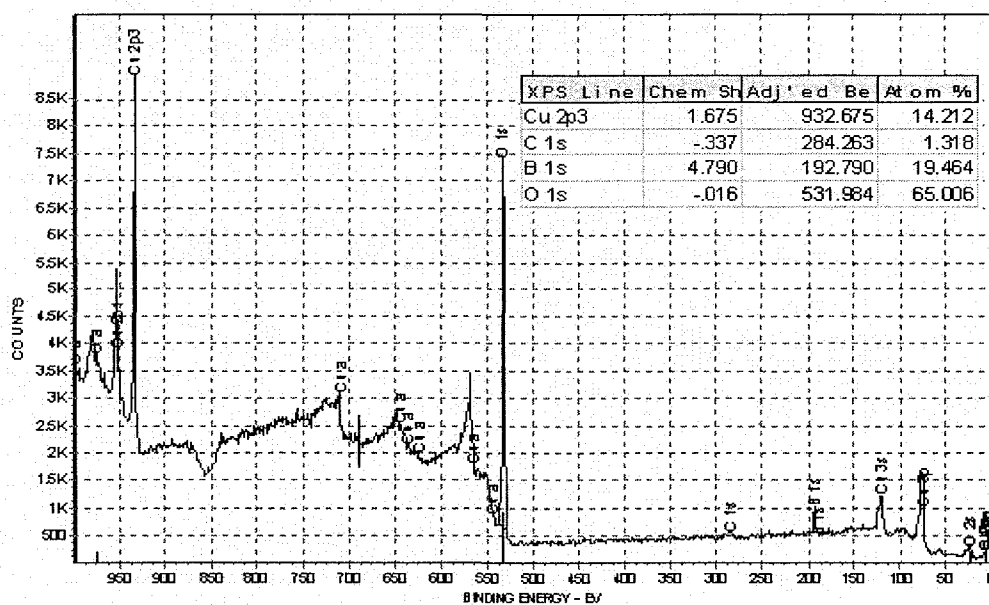


Figure 6. 7 XPS spectra of binding energy versus counts for a typical sample with the glass ring.

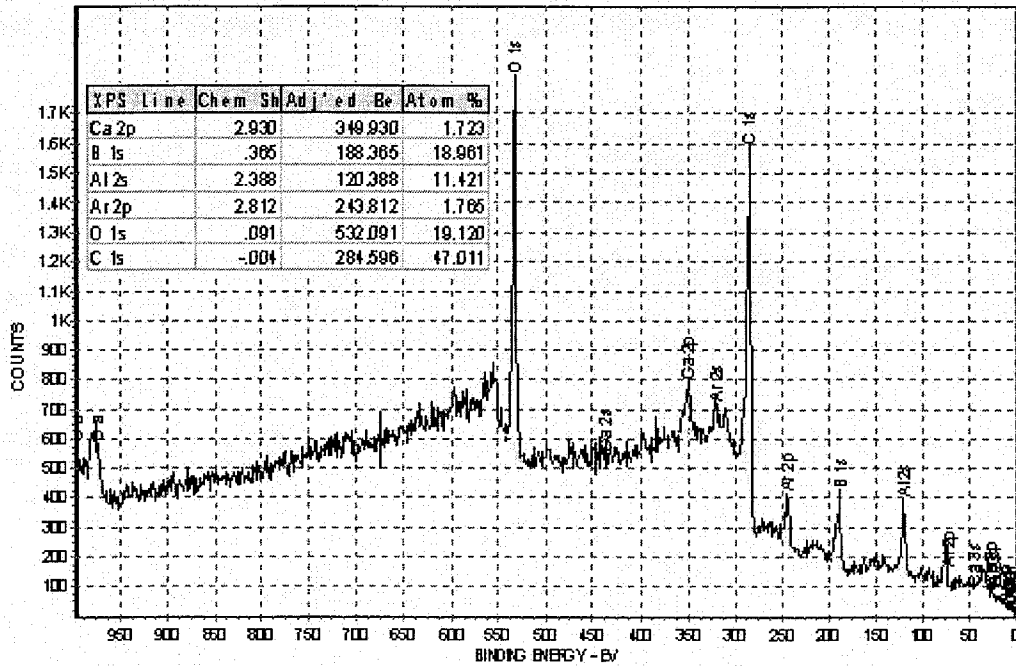


Figure 6. 8 XPS spectra of binding energy versus counts for hemispherical ^{10}B target.

IV Quadrupole gas analyzer

The quadrupole gas analyzer spectrum (Figure 6.9, 6.10 and 6.11) is a plot of $\frac{\text{Mass}}{\text{Charge}} \left(\frac{m}{q} \right)$ versus partial pressure. It is observed from Figure 6.9 that when there is argon flow in the chamber, a high argon peak was observed. A high oxygen peak at $\left(\frac{m}{q} \right)$ of 18 and a vertically small Ar peak at $\left(\frac{m}{q} \right)$ of 40 are observed in the spectrum, when there is no argon flow as seen in Figure 6.10. When the system was pumped without Ar flow for sometime, it is observed that there is no Ar peak, but a persistent oxygen peak as shown in Figure 6.11. The peaks in Figure 6.10 and 6.11 are identified in Figure 6.9. The total pressure of the system was not calibrated therefore, the number on the top right

corner of the spectrum has no quantitative significance where is the peak partial pressures are calibrated and hence can be used for calculations.

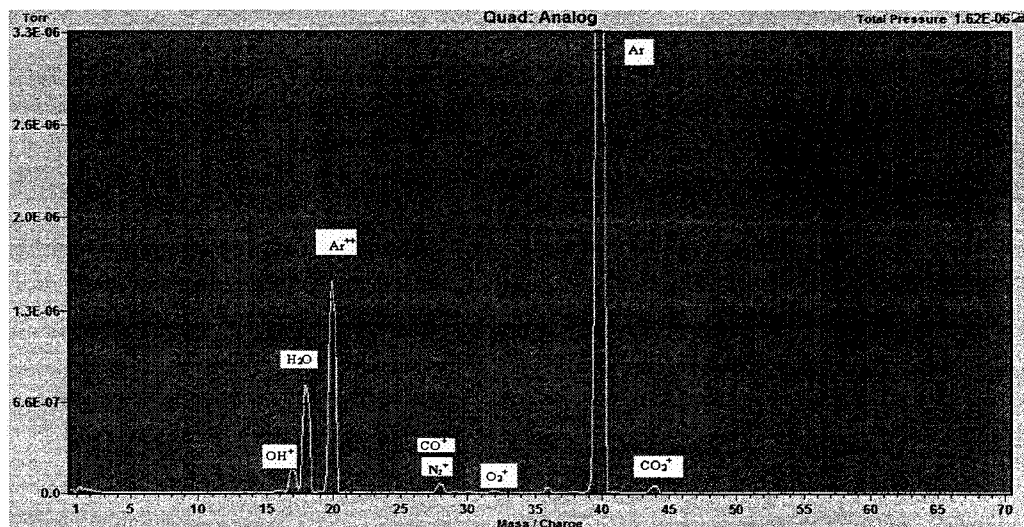


Figure 6. 9 Quadrupole gas analyzer spectrum of $\frac{\text{Mass}}{\text{Charge}}$ ratio versus partial pressure with Ar flow.

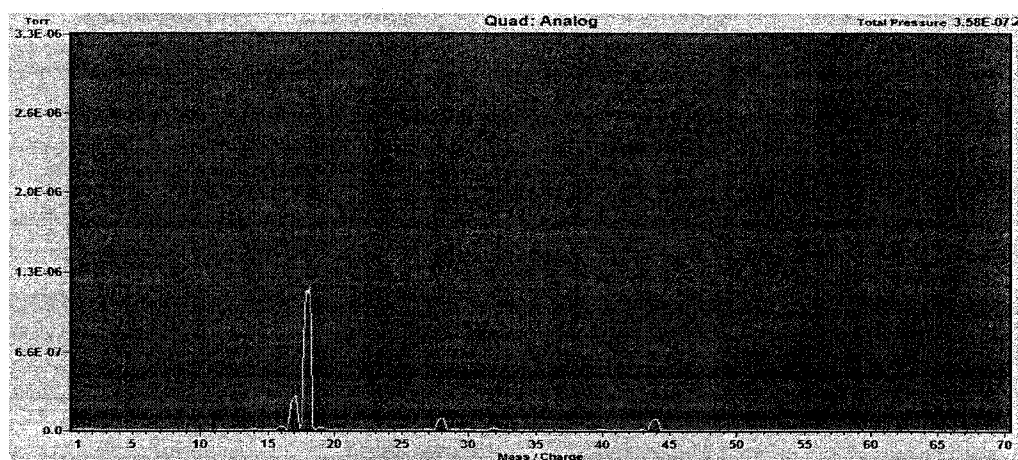


Figure 6. 10 Quadrupole gas analyzer spectrum of $\frac{\text{Mass}}{\text{Charge}}$ ratio versus partial pressure without Ar flow.

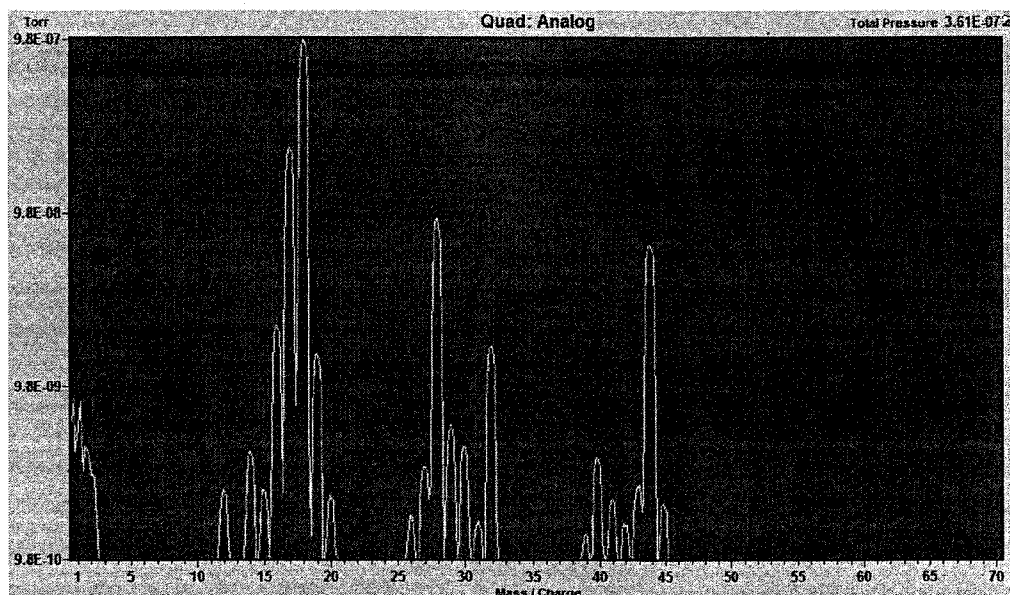


Figure 6. 11 Quadrupole gas analyzer spectrum of $\frac{\text{Mass}}{\text{Charge}}$ ratio versus partial pressure without Ar flow for a long time.

6.2 Discussion

From the results presented in section 6.1, the following conclusions were arrived at:

- The films deposited without glass ring covering the steel cylinder shown in Figure 6.5, contains Fe sputtered from the steel.
- The films deposited with the glass ring covering the steel cylinder shown in Figure 6.6, does not contain Fe sputtered from the steel. The film also does not contain any constituents of glass. This is because as the ions impinge on the glass, it charges up the ring, as glass is a poor conductor of electricity. These initial build up of charge is sufficient to repel ions from the glass surface. It is not clear if the charge dissipation from the glass ring happens within one DC pulse width.

- The deposition conditions for with and without ring were changed from a pressure of 10mtorr to 25mtorr. This is because of change of the electrical impedance of sputter head and charging effect of the glass ring.
- The sputtered film is not uniform in thickness. This is definitely a result of non-uniform sputtering from the target which in itself is a result of non-uniform electric and magnetic field patterns as shown in Figures 5.9 and 5.10. This problem can be overcome by rotating the substrate.
- The sputtered film (with the glass ring) contains a large concentration of oxygen. Results of RGA gas spectrum analyzer shows that this is a result of residual water vapor in the system. The following theoretical estimate of oxygen content to be present in the film based on RGA data shows that the origin of the oxygen in the film is due to the residual water vapor.
- Although a partial pressure of water of about 10^{-6} torr seems very low, water vapor in plasma disassociates easily and the O and OH ions are very reactive. Even the water molecule itself is very reactive. This depends on whether the surface can react. Boron does oxidize. Boron carbide does also, but the carbon goes off as CO and CO₂. If it is assumed that every molecule of water that strikes the freshly forming Boron film does react, it would completely cover the new film with oxide every second. Since the total film thickness of 1 μm (10,000Å) which corresponds to about 3,000 monolayers, was formed at the rate of only 3 Å per second (assuming a 1 hour deposition time), it is expected that 1/3 of the film is oxidized. But it is also possible that the target was partially oxidized to begin with, since it is made of sintered powder, the starting material had a very large

surface area. Furthermore, as the target heated up, its surface would oxidize due to the water vapor.

- From the RGA analysis, it can be observed that origin of oxygen could be from water, oxygen molecule, carbon monoxide and carbon dioxide. It is assumed that the main source of oxygen is from water vapor. Due to lack of knowledge of sticking coefficient of oxygen from the water molecule, it is assumed to be 1. Two independent calculations-one based on total deposition rate and XPS data and the other based on partial pressure data from the RGA gas analyzer, were performed. The details are presented below.

CALCULATION 1: (Based on partial pressure data from RGA)

From the kinetic theory of gases (which is an assumption), the flux density

J_{H_2O} ($\frac{\text{molecules}}{\text{cm}^2 \cdot \text{sec}}$) is related to the partial pressure of H_2O , P_{H_2O} ($\frac{N}{m^2}$) as:

$$J_{H_2O} = \frac{P_{H_2O}}{\sqrt{2 \pi m_o k_B T}} \dots \dots \dots 6.1$$

where m_{H_2O} , is the molecular weight of oxygen, k_B is the Boltzmann constant

which is equal to $1.3806503 \times 10^{-23} \left(\frac{J}{o_K} \right)$ and T is the absolute temperature. Assuming

that the oxygen atoms form a square lattice configuration of size $r_o \times r_o$, where r_o is the ionic radius of oxygen, which is 2.76×10^{-8} cm, number of oxygen atoms arriving per second in the square area can be obtained as:

$$\frac{\text{Number of atoms}}{\text{Sec}} = J_{\text{H}_2\text{O}} A \dots\dots\dots 6.2$$

where $A = r_o \times r_a = (2.76 \times 10^{-8})^2 \text{ cm}^2$. Note that Equation 6.2 represents the deposition rate of water molecule, $D_{\text{H}_2\text{O}}$, and equivalently the deposition rate of oxygen atoms in to the film, D_o . This is true because every molecule of H_2O is assumed to give rise to an atom of oxygen. Using Equations 6.1 and 6.2 and the $P_{\text{H}_2\text{O}}$ data from RGA gas analyzer (partial pressure of water from RGA data was found to be 1.1×10^{-6} torr), the deposition rate of oxygen from water molecule, D_o is obtained as:

$$D_o = 0.010 \frac{\text{atoms}}{\text{sec}} \dots\dots\dots 6.3$$

CALCULATION 2: (Based on total deposition rate and XPS data)

From the XPS data of ^{10}B and O contrast of Figure 6.8, and the ionic radii of O and ^{10}B , the average ionic radius for the film is

$$r_{\text{avg}} = \frac{(\% \text{ of Oxygen})r_o + (\% \text{ of Boron})r_a}{100} = 2.21 \text{ \AA} \dots\dots\dots 6.4$$

From the measurement of thickness of the film and growth time, the total growth rate is found to be 0.046 \AA /sec . Using equation 6.4 and the total growth rate, deposition rate of oxygen, D_o is found to be 0.017 \AA/sec . The agreement between the deposition

rates of oxygen obtained from calculation 1 and 2 is satisfactory considering the various simplifications and assumption made. Thus, it can be reasonably concluded that the predominant source of water oxygen in the film is residual water vapor in the chamber.

- The problem of water vapor in the chamber and hence, the presence of oxygen in the film can be avoided if the chamber can be baked at 150°C for 24 hours. Unfortunately, this is not possible with the current set-up because, there are two rubber o-ring, which cannot be heated above 50°C.

CHAPTER 7

CONCLUSION AND RECOMMENDATIONS

7.1 Conclusions

A DC magnetron sputtering system was designed and built for a ^{10}B hemispherical target. Thin films of ^{10}B were deposited using the hemispherical ^{10}B target in Argon plasma. Initially, the deposited films contained a large percentage of Iron resulting from the exposed rim of the steel cylinder, which is a part of the sputter head housing. Attaching a glass ring to the exposed rim of steel cylinder completely eliminated Iron from the deposited film. The films deposited after the modifications, contained approximately 19.46 % ^{10}B and 65 % oxygen. Also, the thickness of the film was found to be in the range of $1\mu\text{m}$ using SEM. Even though the vacuum system was found to be leak tight based on measurements performed using a quadrupole mass analyzer, the presence of oxygen in the deposited films could not be avoided. This was hypothesized to be due to residual water vapor and our necessarily low deposition rate. This hypothesis was proved to be reasonable estimate from kinetic theory of gases and growth rate and composition measurements.

7.2 Recommendations for Future Work

Based on our experience with the project, the following issues are recommended for further investigation:

- Substrate can be rotated to get a uniform deposition. The speed of rotation can be varied to identify the optimal speed to achieve the best compositional and thickness uniformity.
- The vacuum system can be redesigned to avoid use of the rubber o-rings. The vacuum chamber without rubber o-ring can be baked in order to get rid of the water vapor from the system. This step will eliminate oxygen content of the deposited films considerably.
- Target can be water cooled to prevent the surface heating of the target. This step will allow the changing of operating electrical conditions of the system to increase the deposition rate. This, in turn, will improve the quality of the films by minimizing incorporation of the impurities and oxygen from the chamber.

APPENDIX

I EVACUATION PROCESS

1. Make sure the NEEDLE (A) valve is closed.
2. Open the VENT (B) valve.
3. Open the FORLINE (C) valve.
4. Open the chamber (D) and place the sample (Silicon Wafer) inside.
5. Close the VENT valve.
6. Start the ROUGHING (E) pump.
7. Open the NEEDLE valve. (To evacuate the argon line)
8. Close the NEEDLE valve.
9. Open the Argon valve (F). (Set the Argon pressure to 16psi)
10. Start the TURBO (G) pump. Wait till it reaches 56KRPM.
11. Turn ON the Ionization gauge (H).
12. Wait till the pressure reaches 2×10^{-5} torr and then turn OFF the gauge.

II PLASMA INITIAZION AND SPUTTERING PROCEDURE

1. Open the NEEDLE valve and set the chamber pressure to 25mtorr.
2. Check for open circuit before starting the experiment using a multimeter. If the multimeter indicates a short, then make sure the sputter head does not touch the chamber walls. This is particularly a problem in our system as the sputter head is vertically suspended from the top using a copper rod which can bend relatively easy

3. Turn ON the power supply (I). (Set the mode to current regulation, current to 0.010A and ramp time to 10 seconds)

4. A purple glow around the hemispherical target indicating the existence of Ar plasma.

III TO SHUT DOWN THE PROCESS

1. Turn OFF the power supply.

2. Close the NEEDLE valve. (Do not close the needle valve completely, make sure the pressure gauge reading is 1mtorr)

3. Turn OFF the TURBO pump.

4. Slow down the TURBO by allowing some argon inside.

5. Close the Argon valve.

6. Turn OFF the ROUGHING pump.

7. Vent the chamber by opening the NEEDLE valve.

8. Open the VENT valve to vent the chamber completely.

9. Open the Chamber and remove the sample.

IV POST PROCESSING OF THE SAMPLE

1. Place the sample in the oven after removing it from the chamber.

2. Bake the sample for 15 minutes at 175 degree centigrade.

3. Then, allow the sample to cool down for 30 minutes.

4. Now the sample is ready for characterization.

BIBLIOGRAPHY

- [1] www.sns.gov
- [2] G.F. Knoll, "Radiation Detection and Measurement", Chapter 14 and 15, John Wiley and Sons, second edition.
- [3] W. D. Allen, "Neutron Detection", Philosophical Library, Inc., 1960.
- [4] A. Lorenz, "A Review of Neutron Detection Methods and Instruments", UCID-16325 (1973).
- [5] McGregor D S, Vernon S M, Gersch H K, Markham S M, Wojtczuk S J and Wehe "Self-biased boron-10 coated high-purity epitaxial GaAs thermal neutron detectors" IEEE Trans. Nucl. Sci. 47(2000) 1364–70
- [6] "Roadmap for High Efficiency Solid-State Neutron Detectors", R.J. Nikolic, C.L. Cheung, C.E. Reinhardt, and T.F. Wang, SPIE - International Symposium on Integrated Optoelectronic Devices, Photonics West, Boston, MA, Oct. 2005.
- [7] A. Rose, "Nucl. Instr. and Meth", 52 (1967) 166.
- [8] B. Feigl, H. Rauch, "Nucl. Instr. and Meth " ,61 (1968) 349.
- [9] S. Pospisil, B. Sopko, E. Harrankova, Z. Janout, J. Konicek, I. Macha, J. Pavlu, Radiat. Prot. Dosim. 46 (1993) 115.
- [10] A. Mireshghi, G. Cho, J.S. Drewery, W.S. Hong, T. Jing, H. Lee, S.N. Kaplan, V. Perez-Mendez, IEEE Trans. Nucl. Sci. NS-41 (1994) 915.
- [11] D.S. McGregor, J.T. Lindsay, C.C. Brannon, R.W. Olsen, IEEE Trans. Nucl. Sci. NS-43 (1996) 1357.

- [12] C. Petrillo, F. Sacchetti, O. Toket, N.J. Rhodes, "Nucl. Instr. and Meth", A 378 (1996) 541.
- [13] A.R. Dulloo, F.H. Ruddy, J.G. Seidel, "Radiation response testing of silicon carbide semiconductor neutron detectors for monitoring thermal neutron flux", Report No. 97-98 TK1-NUSIC-R1, Westinghouse STC, 1997.
- [14] F. Foulon, P. Bergonzo, A. Brambilla, C. Jany, B. Guizard, R.D. Marshall, Proc. MRS 487 (1998) 591.
- [15] D.S. McGregor, S.M. Vernon, H.K. Gersch, S.M. Markham, S.J. Wojtczuk, D.K. Wehe, IEEE Trans. Nucl. Sci. NS-47 (2000) 1364.
- [16] R.J. Nikolic, C.L. Cheung, C.E. Reinhardt, T.F. Wang, "Roadmap for High Efficiency Solid-State Neutron Detectors", Optics East, Boston, MA, United States, July 14, 2005
- [17] www.nasa.gov/mission_pages/themis/auroras/sun_earth_connect.html
- [18] N. Tsoulfanidis, "Measurement and detection of radiation", pp. 131-137, Taylor & Francis, Washington, 1995.
- [19] G.E. Thomas, "New technique for producing thin boron films", Nuclear Inst. Methods in Physics Research A, 282, pp. 124-127, 1989.
- [20] Y. Kumashiro, K. Sata, S. Chiba, D. Yamada, K. Tanaka, T. Huodo, K. Yokoyama, and K. Hirata, "Preparation of boron and boron phosphide films by photo- and thermal chemical vapor deposition process", J. Solid State Chem., 154, pp. 39-44, 2000.
- [21] H.K. Gersch, D.S. McGregor, P.A. Simpson, "Nucl. Instr. and Meth", A 489 (2002) 85.
- [22] Se-Hwan Park, Yong Kyun Kim, and J. K. Kim, "Neutron Detection with a GEM",

- [23] Wolf, "Microchip Manufacturing", Lattice Press, 2004.
- [24] www.wikipedia.org
- [25] www.nrl.navy.mil
- [26] R.W.Grove, "On the Electro-Chemical Polarity of Gases", Phil.Trans.Roy.Soc. (London), Vol.142, pp.87-101, 1852.
- [27] Dong-Won Park, "Structure property relationship in longitudinal thin film magnetic recording media", 2006.
- [28] Luis Manuel Angelats Silva, "Study of structural, electrical, optical and magnetic properties of ZnO based films produced by Magnetron sputtering", 2006
- [29] R. B. Heller, J. McGannon, and A. H. Weber, J. Appl. Phys. 21, 1283 (1950).
- [30] www.nat.vu.nl
- [31] www.micromagazine.com
- [32] www.mpi-pse.com
- [33] 34th and 35th Sputter Schools, Rome, Italy Jun., 1984, Santa Barbara, Calif., Nov. 1984.
- [34] Gerhard Lewin, "An Elementary introduction to vacuum technique", AVS, 1987
- [35] Mike Benapfl, "An Overview of Applied Vacuum Technology"
- [36] www.beach-russ.com
- [37] www.bookrags.com
- [38] www.advanced-energy.com
- [39] www.maeresearch.com
- [40] www.chem.qmul.ac.uk

- [41] www.thinksrs.com
- [42] www.extorr.com
- [43] www.answers.com
- [44] www.ucr.edu
- [45] www.geos.ed.ac.uk
- [46] www.capovani.com
- [47] www.ptb-sales.com
- [48] www.inxs-inc.com
- [49] www.semicon.web.net
- [50] www.inficon.com
- [51] www.cosmiclight.com
- [52] www.lowener.se

VITA

Graduate College
University of Nevada, Las Vegas

Priya Raman

Local Address:
1688 Crow Creek Avenue
Las Vegas, NV, 89123

Degrees:
Bachelor of Engineering in Electronics and Communication Engineering,
Bharathidasan University, Trichy, India.

Thesis Title:
Design of Sputtering System for Hemispherical Boron 10 Target.

Thesis Examination Committee:
Chairperson, Dr. Rama Venkat, Ph. D.
Committee Member, Dr. Henry Selvaraj, Ph. D.
Committee Member, Dr. Paolo Ginnobi, Ph. D.
Graduate Faculty Representative, Dr. Clemens Heske, Ph. D.